An improved nanobody-based approach to capture and visualize specific interaction networks of binary protein complexes in living cells

Nawal Hajj Sleiman[1], Julie Carnesecchi[1,2], Yunlong Jia[3], Fréderic Delolme[4], Laurent Gilquin[1], Patrice Gouet[5] and Samir Merabet[1,#]

[1]*Institut de Génomique Fonctionnelle de Lyon, CNRS UMR5242, ENS de Lyon, Université Lyon I, Lyon, France.*

[2]*Institut de Génétique Moléculaire de Montpellier, CNRS, Université de Montpellier, Montpellier, France.*

[3]*Department of Developmental and Cellular Biology, University of California Irvine, Irvine, CA 92697, USA.*

[4]*Protein Science Facility, CNRS-UAR3444, INSERM-US8, École Normale Supérieure de Lyon, Université Lyon I, Lyon, France.*

[5]*Molecular Microbiology and Structural Biochemistry, CNRS UMR5086, Université Lyon I, Lyon, France.*

[#]*corresponding author: samir.merabet@ens-lyon.fr*

Abstract

Protein interaction networks (or interactomes) are formed progressively, each interaction influencing the next one. Accordingly, a same protein will establish different interactomes depending on its first associated cofactor, thereby diversifying its function in the cell. In contrast to their central role, few methods exist to capture interactomes of dimeric protein complexes. Here, we tackle this issue by introducing an innovative method based on bimolecular fluorescence complementation and the specific binding of a nanobody fused to a proximity-dependent biotinylating enzyme. This method was applied to visualize and capture specific interactions of the cytoplasmic TAZ/14-3-3e and nuclear TAZ/TEAD2 complexes, which are major downstream effectors of the Hippo signaling pathway. Among other interactions, we identified SERPINB4 as a novel regulator of TAZ and 14-3-3e proliferative activity in mesenchymal stromal cells. Molecular dissections in living cells revealed the central role of a unique residue of TAZ for recruiting SERPINB4 specifically in the presence of 14-3-3e. Overall, our work demonstrates the importance of considering binary protein complexes for deciphering interactomes and establishes a novel sensitive method in this perspective.

Key words: Bi-nano-ID, BiFC, GFP-nanobody, TurboID, TAZ, Hippo, SERPINB3/4

Introduction

Proteins do not work individually within the cell environment, but by forming connected networks, or interactomes, with other protein-binding partners. These molecular networks are established by successive protein-protein interactions (PPIs) and will vary depending on the cell type and/or cell compartment. This molecular versatility is at the basis of protein function diversification [1]. In addition, transient and low-affinity PPIs are central for shaping interactome identity *in vivo*. Therefore, capturing weak PPIs has become a technological challenge for understanding protein function in normal or pathological conditions [2].

The conventional technique to identify endogenous interactomes of a protein of interest (POI) is affinity purification (AP) and the identification of interacting proteins by liquid chromatography followed by tandem-mass spectrometry (LC/MS-MS). However, AP-based approaches are biased towards direct, high affinity and stable PPIs [3]. The recent development of several proximity-dependent labeling (PL) methods in living cells partially addressed the difficulty to capture low affinity and transient PPIs. These methods take advantage of promiscuous enzymes fused to the POI that can label proximal endogenous proteins (within a radius of approximately 10 nanometers), including transient and weak interaction partners. Although different types of labeling reactions have been described, the most widespread approaches rely on the covalent binding of the small biotin molecule, allowing single-step streptavidin AP before subsequent MS analysis of labelled proteins [3]. One of the recent and most commonly used biotin-based proximity labeling enzymes is the TurboID, which is a directed-evolution variant of the original BioID, with less toxicity, smaller size and considerably faster labeling activity [4]. Split forms of TurboID (split-TurboID) have also been developed to capture interactions of a dimeric protein complex, allowing probing the proteomic composition in a subcellular compartment [5] or cell surface environment [6,7] and identifying SUMO-dependent interactions [8]. However, the activity of the reconstituted TurboID is relatively low compared to the full length/uncut form [5]. Consequently, it requires long incubation times with the biotin (24 hours), which forbids having access to interactome temporal dynamics. Moreover, biotin ligases do not allow observing PPIs in a living cell context.

In this work, we develop a methodology called Bi-nano-ID (**bi**molecular fluorescent complementation (BiFC)-directed **nano**body coupled to proximity **id**entification enzyme). This method aims at specifically characterizing endogenous interactomes of a specific dimeric

68 bait protein complex. Bi-nano-ID was also established with a combination of fluorescent
69 protein fragments that are compatible for doing bicolor BiFC. This property allows to
70 simultaneously visualize the interaction of the novel candidate partner together with the
71 dimeric bait protein complex in the living cell.

72 As a proof of concept, Bi-nano-ID was established by using TAZ (Transcriptional
73 Coactivator with PDZ-binding motif, also named WWTR1) associated to two different
74 cofactors. TAZ (and another functionally related protein called Yes-associated protein, YAP)
75 plays pivotal roles as a downstream component of the Hippo signaling pathway, with a well-
76 known nucleocytoplasmic shuttling property in cells [9]. When the Hippo signaling is active,
77 upstream kinases phosphorylate TAZ, leading to its retention in the cytoplasm and interaction
78 with 14-3-3 proteins. Cytoplasmic TAZ/14-3-3 complexes can promote proliferation and the
79 differentiation of various tissue types [10]. Upon Hippo signaling inactivation, TAZ
80 translocates into the nucleus and interacts with TEAD proteins to bind DNA, resulting in the
81 expression of several target genes. TAZ/TEAD complexes are required for the differentiation
82 of osteoblasts and other cell types [11,12]. Aiming to verify the applicability of Bi-nano-ID,
83 we mapped the interactome of TAZ associated with either the long isoform of 14-3-3 (14-3-
84 3e, also named YWHAE) or the isoform 2 of TEAD (TEAD2) in human HEK293T cells. These
85 two isoforms have been described to regulate the hippo pathway in different cell contexts,
86 including cancers (see for example [13–15]). The role of a novel specific candidate partner of
87 TAZ/14-3-3e complexes was further confirmed at the functional and molecular levels,
88 revealing an unexpected level of interaction plasticity in TAZ and 14-3-3e proteins.

89 Overall, our work demonstrates that Bi-nano-ID is a sensitive method for deciphering
90 interactomes of specific binary protein complexes in living cells.

91

92 **Results**

93 **Capturing the generic interactome of TAZ in living HEK293T cells**

94 Given that we aimed at establishing Bi-nano-ID by considering TAZ associated with either a cytoplasmic
95 or a nuclear cofactor in HEK293T cells, we first asked for the general interaction properties of TAZ in the
96 same cell context. To this end, we generated a TAZ-TurboID fusion construct under the control of a
97 doxycycline (dox)-inducible promoter (see Material and Methods). We assumed that proteins that will be
98 biotinylated by TAZ-TurboID will represent the generic interactome of TAZ, therefore all possible
99 interactions without considering their dependency towards a specific TAZ-associated cofactor
100 (Fig. 1A). In addition, getting the global interactome of TAZ-TurboID expressed in HEK293T

101 cells was also a prerequisite to confirm that this cell line was appropriate for revealing
102 functionally relevant interactions, *i.e.* interactions involved in the Hippo signaling pathway.
103 The expression and activity of TAZ-TurboID was first verified by fluorescent
104 immunostaining (Fig. 1B). Control of specificity was performed with the expression of
105 TurboID alone. This experiment showed strong biotinylation activity in the context of the
106 fusion with TAZ, while weak signals were observed with TurboID alone (Fig.1B and S1).
107 Staining also revealed a preferential localization and biotinylation activity of TAZ-TurboID in
108 the cytoplasm of HEK293T cells (Fig. 1B). Western blots (WB) confirmed the specificity of
109 TAZ-TurboID when compared to TurboID upon AP of biotinylated proteins (Fig. 1C and S1).
110 Altogether, immunostaining and AP experiments validated the specific activity of TAZ-
111 TurboID, and we next performed cell protein extracts for LC/MS-MS analysis with three
112 biological replicates of TAZ-TurboID and TurboID (see also Materials and Methods).
113 Principal component analysis (PCA) showed a distinct distribution for TAZ-TurboID
114 and TurboID replicates (Fig. S1). Moreover, the overlap between the three TAZ-TurboID
115 replicates was high (between 71% to 79% of interactions were common between two replicates,
116 and between 30% to 40% of interactions were common to the three replicates (Fig. S1).
117 All TAZ-TurboID interactions common to at least two different biological replicates
118 and not found with TurboID alone were considered, leading to a total number of 243 proteins
119 (Table S1). We compared this list to the 379 known physical interactors of TAZ described in
120 the literature (https://thebiogrid.org/117434/summary/homo-sapiens/wwtr1.html). Most of
121 these known physical interactors of TAZ have been identified by systematic AP-MS profiling
122 of C-terminally FLAG-HA-tagged bait proteins expressed in HEK293T cells [16]. 66
123 interactions were present in the two lists. Importantly, one of the most enriched GO terms for
124 the 66 common interactors relates to the Hippo signaling pathway (Fig. S1 and Table S1).
125 Interestingly, biological functions associated with the hippo signaling pathway were also
126 enriched when considering the remaining 177 interactions of TAZ-TurboID but not when
127 considering the remaining 275 known interactions (Fig. 1D, S1 and Table S1). Other GO terms
128 related to the hippo pathway were also enriched in the 66 common and 177 TAZ-TurboID
129 interactions (such as cell polarity, cell-cell junction and RNA processing: Fig. 1D and S1),
130 further reinforcing the functional relevance of the two lists.
131 We next selected 6 known and 6 novel TAZ interactors for performing individual
132 Bimolecular Fluorescence Complementation (BiFC) in live HEK293T cells (see Materials and
133 Methods). BiFC relies on the property of monomeric fluorescent proteins to be reconstituted
134 upon complementation when the two sub-fragments are closed enough in space ([17]). It allows

135 assessing whether two candidate proteins could be part of the same protein complex with a
136 simple readout (apparition of a fluorescent signal upon excitation, Fig. 1E-E'). BiFC confirmed
137 that all tested candidates could interact with TAZ. Interaction profiles were diverse although a
138 majority were located in the cytoplasm, which was somehow consistent with the preferential
139 localization and biotinylation activity of TAZ-TurboID in HEK293T cells (Fig. 1F and S1).
140 Altogether, these results showed that AP of biotinylated proteins in HEK293T cells was
141 appropriate for revealing a generic TAZ interactome with functionally relevant GO term
142 enrichments. The validation of the TurboID efficiency in HEK293T to capture TAZ generic
143 interactome allowed the implementation of this biotinylation-based approach for establishing
144 the Bi-nano-ID tool. Moreover, TAZ generic interactome will serve as a reference for further
145 analyses of the specific interactomes of TAZ associated with its cofactors (TAZ/14-3-3e and
146 TAZ/TEAD2 interactome).
147
148 **Establishing Bi-nano-ID experimental parameters in HEK293T cells**
149 Bi-nano-ID is based on an anti-GFP nanobody that will specifically recognize a BiFC complex
150 on the one side, and the coupling to the TurboID enzyme on the other side (Fig. 2A). More
151 particularly, the nanobody (named conditionally stable (cs) GFP-Binding Peptide, csGBP) has
152 been engineered to be unstable when unbound to its epitope, allowing getting a better signal-
153 to-noise ratio, and was originally described in the context of BiFC resulting from the
154 complementation between the N-terminal (0-155: VN155) and C-terminal (156-239: VC)
155 fragment of Venus (a derivative of the yellow fluorescent protein YFP, [18]). The same GFP
156 lacking the conditionally stable mutations, has also previously been used to capture interactions
157 of Venus-based BiFC complexes by immunoprecipitation [19,20].
158 In this work, we aimed at testing the efficiency and specificity of the csGBP nanobody
159 in the context of a complementation system that allows performing bicolor BiFC. This
160 complementation system has been developed to visualize two different PPIs simultaneously,
161 and could serve for the subsequent validation of novel interactions of the dimeric bait protein
162 complex in living cells (Fig. 2B). Bicolor BiFC relies on the property of the N-terminal
163 fragment of YFP (yellow fluorescent protein) to complement with the C-terminal fragment of
164 the blue fluorescent protein ECFP (enhanced cyan fluorescent protein), producing a yellow-
165 like fluorescent signal [21,22]. Two different split sites in the N-terminal fragment of YFP (at
166 the position 155 or 173) can complement with the C-terminal fragment of ECFP (156-239),
167 with the 1-173 N-terminal fragment described to produce stronger fluorescent signals than the
168 1-155 N-terminal fragment [21]. Here, we tested the two complementation sites by using the

169 Venus and Cerulean fluorescent proteins, which display faster maturation time and higher
170 fluorescence brightness than YFP and ECFP, respectively (Fig. S2 and [23,24]). Practically,
171 TAZ was fused to the 155- or 173 N-terminal fragment of Venus (making VN155-TAZ and
172 VN173-TAZ constructs), and the 14-3-3e and TEAD2 cofactors were fused to the 156-239 C-
173 terminal fragment of Cerulean (making CC-14-3-3e and CC-TEAD2 constructs). All
174 constructs were under the same dox-inducible promoter and BiFC was analyzed in living
175 HEK293T cells. Results showed that BiFC obtained with the VN155 fragment was extremely
176 weak when compared to BiFC obtained with VN173, underlining that VN155 could not
177 complement efficiently with the CC fragment in both TAZ/14-3-3e and TAZ/TEAD2
178 complexes (Fig. S2). BiFC with VN173-TAZ also validated the correct cytoplasmic or nuclear
179 localization of TAZ/14-3-3e and TAZ/TEAD2 complexes in live HEK293T cells, respectively
180 (Fig. S2). Collectively, these experiments confirmed that the VN155 fragment was not best
181 appropriate for doing bicolor BiFC and we thus decided to establish Bi-nano-ID by using the
182 VN173 fragment.
183 The specificity of the csGBP-TurboID nanobody was first evaluated by
184 immunofluorescence. BiFC constructs were co-transfected with csGBP-TurboID encoding
185 plasmid, induced with dox, and biotin was added before visualizing both BiFC and
186 biotinylation (see Materials and Methods). These analyses confirmed that BiFC and
187 biotinylation signals colocalized in the case of TAZ/14-3-3e and TAZ/TEAD2 complexes (Fig.
188 2C-D). In contrast, no biotinylation could be observed when expressing the csGBP-TurboID
189 nanobody alone or together with the individual VN173-TAZ, CC-14-3-3e or CC-TEAD2
190 construct, demonstrating that the biotinylating activity was dependent on the binding of the
191 nanobody to BiFC complexes (Fig. S3). Biotinylation signals were also extremely weak in the
192 case of BiFC complexes with VN155-TAZ, underlining that the binding affinity of the
193 nanobody was dependent on the complementation efficiency between the N- and C-terminal
194 fragments (Fig. S2).
195 Next, we tested the specificity of our tools upon affinity purification (AP) with
196 streptavidin-coupled beads. We applied the same BiFC and control conditions as described for
197 the immunostaining. Proteins were extracted, purified and revealed after different incubation
198 timepoints with the biotin to select the best experimental condition for having strong BiFC-
199 specific biotinylation signals with a good signal-to-noise ratio. All quantifications were
200 performed by normalizing the AP over the input and the correct expression of each construct
201 was also validated by using an anti-GFP recognizing the VN and CC fragments (Fig.S4).
202 Results showed non-specific biotinylation activity of the nanobody in the absence of any BiFC

203 constructs (first four lanes in Fig. 2E). Importantly, signals were strongly enriched in the
204 presence of BiFC complexes and quantifications showed that the best incubation time was 180
205 min, with no stronger BiFC-specific biotinylation signals at 240 min (Fig. 2E-E' and S4). The
206 specificity of the nanobody was also more precisely quantified by considering each single
207 construct. This analysis showed negligeable biotinylation activity in the case of CC-14-3-3e
208 and CC-TEAD2 constructs (in comparison to csGBP-TurboID alone: Fig. 2E-E' and S4). In
209 contrast, more signal was observed with VN-TAZ alone (in comparison to the csGBP-TurboID
210 alone: Fig. 2E-E' and S4), indicating that the csGBP-TurboID nanobody was weakly
211 recognizing the VN173 fragment. In conclusion, these experiments established the
212 experimental conditions for purifying BiFC-specific interactomes with the csGBP-TurboID
213 nanobody tool. Because of the weak recognition of the VN173 fragment by the nanobody, we
214 also considered VN-TAZ as an additional filtering control for the analysis of BiFC-specific
215 MS data (see below).
216
217 **Using Bi-nano-ID to capture specific interactomes of TAZ/14-3-3e and TAZ/TEAD2**
218 **complexes in living HEK293T cells**
219 Mass spectrometry analysis was performed by using the streptavidin affinity purified fraction
220 of protein extracts from HEK293T cells in the different control and BiFC conditions. Control
221 conditions consisted in the expression of the nanobody alone (to discriminate for the general
222 background of the TurboID enzyme, referred to as csGBP-TurboID), and to the co-expression
223 of csGBP-TurboID with VN-TAZ (to discriminate for the weak affinity of the nanobody to the
224 VN173 fragment). These two control conditions were used to filter interactions obtained in the
225 two BiFC conditions (csGBP-TurboID co-expressed with VN-TAZ and CC-14-3-3e or with
226 VN-TAZ and CC-TEAD2, Fig. S5).
227 Results showed a good reproducibility between the three biological replicates in each
228 experimental condition (between 26% to 51% of interactions were common to at least two
229 replicates, and between 17% to 30% were common to the three replicates: Table S2 and Fig.
230 S5). Interactions present in two or three replicates were considered for subsequent analyses.
231 Interactions with BiFC complexes were filtered with the interactions obtained in the two
232 control conditions, which led to the identification of 96 and 42 candidate interactions for
233 TAZ/14-3-3e and TAZ/TEAD2 complexes, respectively (Materials and Methods, Table S2 and
234 Fig. S5).
235 To better discriminate for TAZ/14-3-3e- and TAZ/TEAD2-dependent interactions, we
236 compared the two BiFC interactomes with the interactome obtained with TAZ-TurboID. This

237 analysis revealed 50 and 30 interactions that were specifically found with TAZ/14-3-3e and
238 TAZ/TEAD2 BiFC complexes, respectively (Fig. 3A and S6). The finding of BiFC-specific
239 interactions underlined that endogenous 14-3-3 and TEAD proteins did not hid all specific
240 binary complex interactions (although half of the 96 interactions of the TAZ/14-3-3e BiFC
241 complex were also captured with TAZ-TurboID).
242 Importantly, the goal of Bi-nano-ID was to capture interactions that will be specifically
243 distributed between the cytoplasmic TAZ/14-3-3e and nuclear TAZ/TEAD2 complexes. The
244 comparison of these two interactomes revealed 32 interactions that were specific of TAZ/14-
245 3-3e and 12 interactions that were specific of TAZ/TEAD2 (Fig. 3A-C and S6). Thus, we
246 concluded that Bi-nano-ID was successful for capturing BiFC-specific interactomes.
247 In order to know the functions that could be associated with the common and/or specific
248 TAZ-related interactomes, we performed a GO-term enrichment analysis (see Materials and
249 Methods and Table S2). "Hippo signaling pathway" was strongly enriched in TAZ/14-3-3e
250 and TAZ/TEAD2 interactomes (in addition to the TAZ-TurboID interactome), emphasizing
251 that our tools led to the capture of functionally relevant interactions (Fig. 3B'-C' and S7).
252 Interestingly, functions related to mRNA stability and catabolic processes were also enriched
253 in the three interactomes, suggesting that they also represent a major and generic molecular
254 facet of TAZ (Fig. 3B'-C' and S7). Several GO terms were specifically associated with
255 TAZ/14-3-3e or TAZ/TEAD2 interactome. Importantly, some of these specific functions were
256 consistent with the known activity of 14-3-3 and TEAD proteins with YAP/TAZ effectors
257 (such as nuclear export and stem cell division for TAZ/14-3-3e, or nuclear import and
258 transcription for TAZ/TEAD2, Fig. 3B'-C'). Other specific functions (like "negative regulation
259 of adipose tissue development" and "circadian rhythm" for TAZ/14-3-3e, or "keratinocyte
260 development" and "odontoblast differentiation" for TAZ/TEAD2) are associated with
261 YAZ/TAZ in the literature (see for example [25–28]). These observations underline that Bi-
262 nano-ID was efficient for capturing novel interactions that could be involved in known specific
263 TAZ/14-3-3e and TAZ/TEAD2 functions. Finally, not all the generic TAZ functions were
264 captured with the TAZ/14-3-3e and TAZ/TEAD2 interactomes (like oocyte maturation or
265 mitophagy regulation, Fig. S7), suggesting that these TAZ functions could rely on other 14-3-
266 3- and TEAD-independent partnerships.
267
268 **SERPINB3 and B4 potentiate the proliferative activity of TAZ and 14-3-3e in HS27A**
269 **mesenchymal stromal cells**

270 YAP/TAZ regulators have context-dependent roles in stem cells, either driving self-renewal or
271 differentiation depending on the identity of the stem cell [29,30]. These differential activities
272 are also linked to the cytoplasmic or nuclear localization, therefore to the association with
273 cytoplasmic (including 14-3-3) or nuclear (including TEAD) cofactors. Here, we wondered
274 whether some specific TAZ/14-3-3e or TAZ/TEAD2 interactions captured with Bi-nano-ID
275 could be functionally relevant in a stem cell-like context. To this end, we considered the HS27A
276 bone marrow mesenchymal stromal cell line that can be induced into different cell types
277 depending on the cell culture medium [31,32]. Given that a common enriched GO term for
278 TAZ/14-3-3e and TAZ/TEAD2 complexes was related to the "positive regulation of osteoblast
279 differentiation" (Fig. S7), we decided to cultivate HS27A cells in an osteoblast-differentiation
280 medium. The differentiation into osteoblast was confirmed with Alizarin red staining (see
281 Materials and Methods and Fig. 4A-A'). We hypothesized that cofactors working in concert
282 with TAZ/14-3-3e or TAZ/TEAD2 complexes could potentially display distinct expression
283 profiles depending on the mesenchymal-like/undifferentiated or osteoblast-like/differentiated
284 state of HS27A cells. In order to identify such candidate cofactors, we performed RNA-seq
285 experiments of HS27A cells at day 1 (proliferation state) and at day 15 (osteoblast
286 differentiation state). RNA-seq data showed several genes that were strongly up- or down-
287 regulated when comparing the proliferative and differentiated state of HS27A cells (Fig. 4B
288 and Table S3). Unexpectedly, neither *TAZ*, nor *TEAD* or *14-3-3* genes showed a significant
289 differential expression level between the undifferentiated and differentiated cell state (Table
290 S3). This observation suggests that their role could depend on post-transcriptional regulatory
291 process, such as the regulation of the nuclear shuttling. Nevertheless, although a number of the
292 genes displaying a differential expression profile could correspond to downstream effectors of
293 TAZ/14-3-3e and TAZ/TEAD2 complexes, we compared the list of differentially expressed
294 genes to our lists of specific candidate cofactors captured with Bi-nano-ID. This analysis led
295 to the identification of *SERPINB3* and *SERPINB4.* Interestingly, these two genes were among
296 the most downregulated genes during the differentiation process, and the corresponding
297 proteins were specifically captured with TAZ/14-3-3e (LC/MS-MS analysis could not
298 discriminate between SERPINB3 and B4, which share 92% identity in their amino acid
299 sequence, Fig. 3B and S8). SERPINB3 and B4 belong to the family of serine/cysteine protease
300 inhibitors and are frequently co-expressed in different tissues. Their physiological role remains
301 largely unknown, but their abnormal elevated expression level has been reported to contribute
302 to several pathologies, including chronic liver diseases, inflammatory diseases and cancer (such
303 as squamous cell carcinomas and primary liver cancers ([33,34]). SERPINB4 has also been

304 associated with psoriasis severity that is characterized by epidermal hyperproliferation and
305 infiltration of inflammatory cells [35]. Moreover, the analysis of the known interactome of
306 SERPINB4 revealed SERPINB3 and two other interaction partners that were specifically
307 captured with TAZ/14-3-3e: S100A8 and S100A9 (Fig. 3B-C and 4C). These two proteins have
308 been described to be part of a common circuit with the hippo signaling and promote the
309 proliferation and colony formation of breast cancer cells [36]. Finally, "stem cell division" was
310 also among the most enriched GO terms specific of the TAZ/14-3-3e interactome (Fig. 3B and
311 Table S2). Altogether, these observations suggest that SERPINB3 and B4 could play a role for
312 the proliferation of HS27A cells, making them strong candidates to test in the context of
313 TAZ/14-3-3e proliferative activity.
314 To test this hypothesis, we generated two different siRNAs targeting *TAZ*, *14-3-3e* or
315 *SERPINB3* and *B4*. The specificity of each siRNA was individually tested in HS27A cells (Fig.
316 S9 and Materials and Methods) and we next assessed their effect on HS27A cells proliferation,
317 either alone or in various heterologous combinations. Results showed that the individual
318 targeting of *TAZ, SERPINB3/B4* or *14-3-3e* affected the proliferation rate of HS27A cells at
319 35h post transfection, and this effect tended to fade over time (at 50h, which could be explained
320 by siRNA dilution over cell generations; Fig. 4D). Importantly, combining siRNAs against
321 *SERPINB3/B4* and *TAZ* or *SERPINB3/B4* and *14-3-3e* already impacted proliferation at 24h
322 post-transfection, and further decreased HS27A proliferation rate when compared to individual
323 siRNAs at 50h (Fig. 4D). These combinatorial effects were similar to the one observed when
324 combining *TAZ* and *14-3-3* siRNAs and were more persistent over time when compared to
325 individual siRNAs (Fig. 4D). These results show that SERPINB3 and B4 are required for the
326 proliferation of HS27A cells and act in concert with TAZ and 14-3-3e. This effect was
327 independent of cross-regulatory relationships given that the knock-down of *SERPINB3* and *B4*
328 had no effect on *TAZ* or *14-3-3e* expression (Fig. S9). We propose that the combinatorial effect
329 of siRNAs could result in a more complete loss of functional protein complex assemblies given
330 that each siRNA was not 100% effective (Fig. S9). In this context, *SERPINB3* and *B4* could
331 have a redundant role for promoting the proliferative activity of TAZ and 14-3-3e through the
332 formation of specific trimeric protein complexes.
333
334 **Specific interaction interfaces allow the formation of trimeric TAZ/14-3-3e/SERPBIN4**
335 **complexes**
336 To understand how SERPINB3 or B4 could form a trimeric complex with TAZ and 14-3-3e,
337 we used the artificial intelligence (AI) platform AlphaFold-multimer to predict hetero-

338 oligomeric structures (https://alphafold.ebi.ac.uk/ and [37]), and the webserver ENDscript to
339 analyze intermolecular contacts [38]. Although the top-ranked predicted model for SERPINB3
340 and B4 had a relatively low interface predicted template modelling (ipTM) score (0,4), as it
341 can be expected because of long disordered regions of TAZ, they both showed the emplacement
342 of a disordered 306-322 C-terminal segment of TAZ in between 14-3-3e and SERPINB3 or B4
343 (Fig. S10-S11). This segment of TAZ contains a short linear interaction motif (SLIM) that
344 could be phosphorylated by LATS kinases ([39–41] and Fig. S10). Importantly, this SLIM is
345 the only contacting region of TAZ with SERPINB3 or B4 (Fig. S10-11). In particular, a unique
346 residue, Glu309, is depicted to contact two Lys residues of SERPINB4 in the trimeric complex
347 with 14-3-3e (Fig. S10 and S11). In contrast, several residues of the SLIM are establishing
348 contacts with 14-3-3e in the same trimeric protein complex (Fig. S10-11). Overall, these
349 predictions highlight that the C-terminal SLIM of TAZ could constitute a central node for
350 making strong interactions with both SERPINB3 or B4 and 14-3-3e in the trimeric complex.
351 To further confirm these predictions, we took advantage of bicolor BiFC to analyze
352 interaction properties between TAZ, 14-3-3e and SERPINB4 in a live cell context. As
353 described previously (Fig. 2B), bicolor BiFC was achieved by co-expressing VN-TAZ and CC-
354 14-3-3e together CN-SERPINB4 to look at the Venus-like (VN-TAZ/CC-14-3-3e) and
355 Cerulean-like (CN-SERPB3-4/CC-14-3-3e) fluorescent signals in living HEK293T cells (Fig.
356 5A). Results showed identical diffuse profiles with few enrichment dots in the cytoplasm for
357 the two BiFC signals, demonstrating that TAZ-14-3-3e and 14-3-3e-SERPINB4 interactions
358 occurred at the same places and could therefore be part of a same protein complex (Fig. 5A').
359 To further confirm that SERPINB4 could interact with both TAZ and 14-3-3e, we performed
360 bicolor BiFC by expressing CC-SERPINB4 together with VN-TAZ and CN-14-3-3e, allowing
361 looking at TAZ-SERPINB4 and 14-3-3e-SERPINB4 interactions in green and cyan,
362 respectively (Fig. 5B). Again, the two BiFC profiles were superposable in the cytoplasm (Fig.
363 5B'), indicating that the two interactions occurred at the same locations within the cell.
364 Altogether, bicolor BiFC observations are in agreement with the potential formation of trimeric
365 TAZ/14-3-3e/SERPINB4 complexes.
366 To assess whether the formation of these trimeric complexes could rely on cooperative
367 interactions between the three partners, we took advantage of BiFC as a simple readout of
368 interaction affinity. More precisely, we first expressed only the VN-14-3-3e and CC-
369 SERPINB4 constructs, which led to Venus-like fluorescent signal (Fig. 5C-C'). We reasoned
370 that these BiFC complexes could potentially be established for their large majority without
371 endogenous TAZ given that BiFC constructs were overexpressed with the dox-inducible

372 promoter and that *TAZ* was weakly expressed in HEK293T cells (as deduced from RNA-seq
373 experiments, Kundlacz et al., in preparation). Accordingly, co-overexpressing a HA-tagged
374 version of TAZ together with VN-14-3-3e and CC-SERPINB4 led to a strong increase of BiFC
375 signals (around 7 folds, Fig. 5C-C"). This observation demonstrates that the formation of a
376 trimeric complex with TAZ promotes the interaction between 14-3-3e and SERPINB4.
377 To also analyze the contribution of 14-3-3e on TAZ-SERPINB4 interaction, we performed
378 BiFC between VN-TAZ and CC-SERPINB4 when affecting endogenous *14-3-3e* (Fig. 5D),
379 which is more strongly expressed than *TAZ* in HEK293T cells (Kundlacz et al., in preparation).
380 We observed that the depletion of endogenous *14-3-3e* (around 60% loss was obtained upon
381 siRNA transfection, S9) led to strong decrease of BiFC signals (around 50% loss, Fig. 5D'-
382 D"). Thus, we concluded that endogenous 14-3-3e was sufficiently highly expressed to
383 participate to the BiFC complexes and promote TAZ-SERPINB4 interaction.
384 Altogether, these experiments established that binary interactions between SERPINB4 and
385 TAZ or SERPINB4 and 14-3-3e were increased in the presence of the third partner, strongly
386 suggesting that TAZ, 14-3-3e and SERPINB4 could establish cooperative interactions to
387 trimeric protein complex.
388 To experimentally validate the predictive interaction interface of TAZ with SERPINB4,
389 we mutated the residue Glu309 into an Alanine residue (construct TAZ^{E309A}), anticipating that
390 this mutation could affect TAZ-SERPINB4 interaction specifically in the context of
391 TAZ/SERPINB4/14-3-3e trimeric complex. Indeed, interaction interfaces are all predicted to
392 be different when comparing the trimeric complex to the different dimeric complexes (Fig.
393 S12-14). Of interest, the residue Glu309 of TAZ is not predicted to contact any SERPINB4
394 residues in the dimeric TAZ/SERPINB4 complex (Fig. S12). These predictions underscore that
395 binary interactions could be completely remodeled in the presence of the third partner.
396 The correct expression and localization of TAZ^{E309A} was verified (Fig. S10) and the effect of
397 the TAZ punctual mutation was analyzed by doing bicolor BiFC to simultaneously analyze the
398 interaction of SERPINB4 with either TAZ^{E309A} or 14-3-3e (Fig. 6A). Results showed 80% loss
399 of BiFC between SERPINB4 and TAZ^{E309A}, thus confirming that the residue Glu309 of TAZ
400 was central for recruiting SERPINB4 in the context of the trimeric complex (Fig. 6A'-A").
401 The inability of TAZ^{E309A} to interact with SERPINB4 was also indirectly demonstrated by the
402 absence of any promoting effect of HA-TAZ^{E309A} when over-expressed with VN-14-3-3e and
403 CC-SERPINB4 (Fig. 6B-B"), indicating that HA-TAZ^{E309A} lost most of its ability to form a
404 trimeric complex with SERPINB4 and 14-3-3e.

405 Surprisingly, bicolor BiFC in the context of VN-TAZ^{E309A} also showed a strong
406 decrease (around 50%) of signal between CN-14-3-3e and CC-SERPINB4 (Fig. 6A'-A").
407 Thus, the loss of interaction between TAZ^{E309A} and SERPINB4 also affected the interaction
408 between SERPINB4 and 14-3-3e, underlining that the interaction interfaces between these two
409 proteins was remodeled (and with a lower affinity) when TAZ was not interacting with
410 SERPINB4.
411 To further confirm that interaction interfaces are different when considering the trimeric and
412 dimeric complexes, we analyzed the effect of the mutation of the Glu309 residue of TAZ in
413 the absence of 14-3-3e. To this end, we repeated the analysis of BiFC between VN-TAZ^{E309A}
414 with CC-SERPINB4, in wild type condition or by simultaneously expressing *14-3-3e* siRNA
415 to affect endogenous 14-3-3e (Fig. 6D). First, we observed BiFC despite the presence of
416 endogenous *14-3-3e* in wild type condition (Fig. 6D'). This observation confirmed that VN-
417 TAZ^{E309A}/CC-SERPINB4 dimeric complexes could be formed in excess with regard to
418 endogenous 14-3-3e. Importantly, depleting endogenous *14-3-3e* did not affect the BiFC signal
419 intensity, demonstrating that TAZ^{E309A}/SERPINB4 complexes were formed through distinct
420 and 14-3-3e-independent interaction interfaces as compared to TAZ-SERPINB4 interactions
421 established in the context of trimeric TAZ/SERPINB4/14-3-3e BiFC complexes (Fig. 6D'-D").
422 Collectively, these experiments confirmed that the Glu309 residue of TAZ is critical
423 for recruiting SERPINB4 in the specific context of the trimeric association with 14-3-3e. In
424 addition, this Glu309-dependent interaction allows SERPINB4 to strongly interact with 14-3-
425 3e, thus showing the mutual dependency of each partner to form a cooperative trimeric protein
426 complex.
427
428 **Discussion**
429 In this study, we developed and validated Bi-nano-ID, a novel method that combines BiFC
430 with proximity-dependent biotinylation, to investigate binary protein interactions and their
431 associated interactomes in living cells. By using TAZ/14-3-3e and TAZ/TEAD2 interactions
432 as a proof-of-concept, we demonstrated the efficiency of Bi-nano-ID in capturing and
433 characterizing these interactions within their specific cellular compartments.
434
435 **Advantages of Bi-nano-ID over other experimental approaches and future potential**
436 **improvements**
437 To date, the unique alternative methodologies to capture interactomes of dimeric complexes
438 rely on split-BioID and split-TurboID enzymes, which can be reconstituted upon spatial

439 proximity. These approaches have been used to identify interactomes of different dimeric
440 protein complexes and to monitor [8,42,43] or capture interactions in specific cellular
441 compartments [5]. However, these systems require long biotin incubation times (minimum 8
442 hours) due to the decreased activity of the reconstituted TurboID. In contrast, Bi-nano-ID
443 integrates BiFC, which is well established for providing a specific readout of many different
444 types of PPIs, allowing visualizing and validating the correct interaction profile of the dimeric
445 protein complex in living cells. In addition, the use of a BiFC-recognyzing nanobody fused to
446 full length TurboID enables to exploit the robust and rapid biotinylation capabilities of full
447 length TurboID with shorter time of biotin incubation when compared to split-TurboID
448 systems. Incubation times applied with Bi-nano-ID are still in the range of few hours, but this
449 time could potentially be diminished if it is a critical parameter. For example, in our work we
450 decided for 180min incubation time, but a significant enrichment (also to a less extent) could
451 already be obtained at 90min incubation time (Fig. S4). Getting access to the fine temporal
452 dynamics (range of minutes) of a binary complex interactome will require developing tools
453 with other complementation systems that are reversible (unlike BiFC, see for example [44]).
454 In any case, the Nanobody-TurboID combination constitutes the most sensitive tool for
455 detecting interactions of binary protein complexes within defined subcellular localizations.
456 Finally, by using fragments compatible for bicolor BiFC, Bi-nano-ID allows to rapidly validate
457 candidate proteins of the interactome together with the bait dimeric complex in living cells. In
458 addition, human gene libraires have also been generated in fusion with the CC fragment to
459 perform large-scale BiFC interaction screens in human living cells (*Kundlacz et al. in*
460 *preparation* and [45]). In this context, Bi-nano-ID could help to further characterize the
461 endogenous interactome of the VN-bait protein associated to a candidate CC-cofactor
462 identified from a BiFC interaction screen.
463

464 **Bi-nano-ID identified distinct interaction partners for TAZ/14-3-3e and TAZ/TEAD2**
465 **complexes**

466 Interactions between TAZ and 14-3-3e or TAZ and TEAD2 were visualized using BiFC,
467 showing distinct cytoplasmic and nuclear fluorescence patterns respectively, and confirming
468 their subcellular localization as influenced by the Hippo signaling pathway. This initial
469 validation set the foundation for integrating the csGBP nanobody fused with the TurboID
470 enzyme, which led to the biotinylation of proteins in proximity to the BiFC complexes. The
471 subsequent biotinylation was specific and colocalized with the BiFC signals, as revealed by

472 immunofluorescence and western blot analyses, indicating the precision and reliability of Bi-
473 nano-ID in live-cell contexts.
474 Due to the weak recognition of the VN173 fragment by the csGBP nanobody, we also
475 tested our tools when using VN155-TAZ, which was not recognized by the nanobody in
476 previous work [19]. These assays showed that BiFC was weak and not exploitable with 14-3-
477 3e or TEAD2 fused to the CC fragment. Consequently, biotinylation was also less efficient.
478 We concluded that VN155 was much less appropriate than VN173 in our bicolor
479 complementation strategy, which was also consistent with previous work [45]. In addition,
480 using VN173-TAZ alone as a negative control was efficient for discriminating the background
481 resulting from the weak affinity of the csGBP nanobody for the VN173 fragment in the mass
482 spectrometry analysis.
483 Our work identified a substantial number of proteins in proximity to TAZ/14-3-3e and
484 TAZ/TEAD2 complexes. The stringent filtering process ensured high specificity, leading to
485 the identification of 96 candidates for TAZ/14-3-3e and 42 candidates for TAZ/TEAD2.
486 Further refinement excluded proteins identified with TAZ-TurboID, which were considered as
487 generic interaction partners when compared to interactions that could be established with
488 BiFC-stabilized TAZ/14-3-3e and TAZ/TEAD2 complexes. This filtering step led to the
489 identification of 49 TAZ/14-3-3e interactors and 29 TAZ/TEAD2 interactors. 17 interactions
490 were common to the two complexes, demonstrating that Bi-nano-ID was successful in
491 capturing interactions that were specific of TAZ/14-3-3e (32 interactions) and TAZ/TEAD2
492 (12 interactions). Gene ontology enrichment analyses revealed that TAZ-TurboID, TAZ/14-3-
493 3e and TAZ-TEAD2 interactors all predominantly participate in Hippo pathway regulation,
494 highlighting that these novel interactions could modulate TAZ function. Importantly, TAZ/14-
495 3-3e and TAZ/TEAD2 interactomes displayed clear distinct GO term enrichments, allowing
496 assigning specific functions of TAZ depending on its association with either 14-3-3e or TEAD2
497 cofactors. Collectively, these results demonstrate the suitability of Bi-nano-ID for capturing
498 and distinguishing interactomes of a bait protein associated with a different cofactor in two
499 different cellular compartments.
500
501 **Molecular insights into TAZ/14-3-3e/SERPINB4 complex formation and its biological**
502 **implications**
503 Our detailed molecular dissection using bicolor BiFC and mutagenesis identified a critical
504 interaction interface for both 14-3-3e and SERPINB4 within the TAZ protein. More
505 particularly, this region encompasses residues 306-322 and is predicted to be phosphorylated

506 by LATs kinases, therefore under dynamic regulation depending on the activation of the Hippo
507 pathway. Importantly, mutating the single Glu309 residue of TAZ predicted to form
508 electrostatic interactions with two Lys residues of SERPINB4 was sufficient to abolish all
509 cooperative interactions involved in the trimeric complex assembly. In particular, the
510 Glu309Ala mutation was able to also affect the interaction between 14-3-3e and SERPINB4
511 but only in the context of the trimeric complex, highlighting that 14-3-3e and SERPINB4 have
512 TAZ-dependent and TAZ-independent interaction modes (Fig. 7). Similar interaction
513 properties could apply for TAZ/14-3-3e/SERPINB3 complexes although it remains to be
514 firmly demonstrated. We suggest that the TAZ-dependent mode of interaction, therefore
515 interaction in the context of trimeric TAZ/14-3-3e/SERPINB3/4 complexes, could be more
516 stable and potentiate the proliferative activity of TAZ/14-3-3 complexes (Fig. 7). This
517 hypothesis results from our assays in human bone marrow stromal cells (HS27A) but could
518 potentially apply more generally in cell progression, proliferation and metastasis for cancer
519 biology and tissue regeneration. In this context, the identification of the most relevant
520 interaction interface used in the trimeric and not the dimeric complex could have strong
521 incidence for future therapeutic development.
522 In conclusion, our work highlights the importance of considering interactomes of dimeric
523 protein complexes over single bait proteins, and the relevance of Bi-nano-ID in this
524 perspective.
525
526 **Materials and Methods**
527 **Cell culture**
528 HEK293T cells were purchased from the European Collection of Authenticated Cell Cultures
529 (ECACC) through the biological resource center CelluloNet (AniRA platform of the
530 UAR3444, Lyon, France). Human bone marrow stromal cells (HS27A) were a gift from the
531 team of Dr. Véronique Maguer-Satta (CRCL). HEK-293T cells were cultured as a monolayer
532 in Dulbecco's modified Eagles medium (DMEM-GlutaMAX-I, Gibco by Life Technologies)
533 supplemented with 10% (*v/v*) heat-inactivated fetal bovine serum (FBS) (Gibco by Life
534 Technologies), 1% (*v/v*) Penicillin-Streptomycin (5,000U penicillin and 5mg
535 streptomycin/mL, Gibco), and 5 ml of 100 mM sodium pyruvate (Gibco by Life Technologies)
536 incubating at 37°C, in an atmosphere of 5 % CO_2. HS27A cells were cultured in RPMI 1640
537 (Gibco by Life Technologies) supplemented with 10% (*v/v*) heat-inactivated fetal bovine serum
538 (FBS) (Gibco by Life Technologies) and 1% (*v/v*) Penicillin-Streptomycin (5,000U penicillin
539 and 5mg streptomycin/mL, Gibco) incubating at 37°C, in an atmosphere of 5 % CO_2.

540

541 **Cloning**

542 Plasmids used in this study were cloned either by gateway cloning or conventional restriction
543 digestion into pLIX _403 vector (a gift from David Root; Addgene plasmid #
544 41395; http://n2t.net/addgene:41395, RRID: Addgene_41395). All constructs are placed under
545 the same tet-off dox-inducible promoter. All constructs were sequenced (Genewiz company,
546 Germany) before using. Oligonucleotides used for the cloning are listed (Table S4).

547

548 **Fluorescent immunostaining**

549 50.10^5 HEK-293T cells were seeded on glass coverslips in 24-well plate for 18-24 hours to
550 about 80% confluency, then transiently transfected with 250 ng of each plasmid using
551 jetPRIME (Polyplus, Ref 114-15) and following manufacturer's instructions in the presence of
552 doxycycline (dox, 100 ng/ml). After 14h of dox induction, cells were washed with PBS and
553 replaced by fresh complete media without dox for 6h at 37°C. Cells were then cultured in 50
554 µM Biotin for 3h at 37°C under 5% CO_2. Cells were then washed twice with 1X PBS and fixed
555 with 4% (*v/v*) paraformaldehyde at 4°C for 15 min. In between each step, cells were washed
556 with 1X PBS. Cells were permeabilized with 0,1% Triton for 10 min followed by a blocking
557 step in 2% (*w/v*) BSA for 1h at RT. Cells were then incubated with primary antibody (Rabbit-
558 anti-GFP A11122 Invitrogen at 1/1000) in PBS supplemented with 2% (w/v) BSA for 3 hr at
559 RT. Next, samples were incubated with anti-rabbit-Alexa Fluor 488 and Alexa Fluor 555-
560 Streptavidin to reveal biotinylated proteins, in PBS supplemented with 2% (w/v) BSA for 1 hr
561 at RT. Finally, cell-coated coverslips were mounted in VECTASHIELD antifade mounting
562 medium with DAPI (VECTOR, Cat No. LS-J1033-10) and imaged by confocal microscopy
563 (Zeiss LSM780).

564

565 **Western blots**

566 Cells were cultured in Biotin (50 µM) at 37°C under 5% CO_2 at several incubation times (10
567 min, 90min, 180min, and 240min). Cells were washed twice with 10 ml ice-cold DPBS,
568 harvested by scraping, pelleted by centrifugation at 1,400 r.p.m. for 3 min, and either processed
569 immediately or stored at -80°C before further analysis.

570 The protocol of TurboID labeling (with TurboID-HA or TAZ-TurboID-HA constructs) is
571 similar to the approach followed for Bi-nano-ID labeling, except that cells were incubated with
572 biotin 50 µM for 10 min.

573 Collected cell pellets for both Western blotting (WB) and proteomic analysis were resuspended
574 in ice-cold RIPA/1%SDS-cell lysis buffer (50mM Tris pH8, 150mM NaCl, 0.5% sodium
575 deoxycholate, 1% NP40/IGEPAL) (volume ratio between cell pellet: buffer = 1:3) and
576 incubated on ice for 20-30 min, maintaining constant vortex (2-3 times). The cells were then
577 treated with Benzonase Nuclease (Sigma, E1014-25KU) for 10 to 20 min on ice or to observe
578 the solution becomes less viscous. This was subjected to spin at 14000×g at 4°C for 10 min.
579 The supernatant was then transferred to 1,5 Eppendorf tube. To test the expression of the
580 constructs, 10% of the protein extracts were kept for WB as input fraction. Proteins were
581 quantified using Pierce BCA Protein Assay (Thermofischer, A55865). Streptavidin magnetic
582 beads (Sigma, 88817) were equilibrated with two PBS washes and resuspended in RIPA buffer
583 supplemented with 1% SDS (50 mM Tris pH 8, 150 mM NaCl, 0.5% sodium deoxycholate,
584 1% NP40, 1% SDS). 1 mg of protein extracts were incubated with 40 µl of streptavidin beads
585 in a final volume of 1 ml RIPA-SDS overnight at 4°C on a rotating wheel. Beads were then
586 washed twice with SDS-Buffer (10 mM Tris.HCl, 1 mM EDTA, 1% SDS, 200 mM NaCl),
587 twice with RIPA-SDS and twice with acetonitrile buffer (20% acetonitrile in MS-grade water).
588 For WB validation, acetonitrile washing step was skipped.
589 For western blot analysis, proteins (Input and AP) were resolved on 12% SDS-PAGE, blotted
590 onto PVDF membrane (Biorad) and probed with specific antibodies after saturation. The
591 antibodies (and their dilution) used in this study were, Histone 3 (1791 Abcam, 1/10,000), GFP
592 (A11122 Life Technologies, 1/1000), and Streptavidin-HRP (SA10001 Invitogen, 1/5000).
593 Developing was performed using chemiluminescence reaction (ECL, Cytiva) with secondary
594 antibody coupled to HRP (Promega, 1/5000).
595
596 **Mass spectrometry preparation**
597 Streptavidin beads were resuspended in 14 µl of ammonium bicarbonate 50 mM and proteins
598 were subjected to reduction with 1 µl DTT (100 µM, 57°C, 45min) and alkylation with 1µl
599 iodoacetamide (500µM, RT, 45min at dark). The proteins were then digested with a mixture of
600 endoproteinase Lys-C/trypsin (ratio protein/enzyme 1/100, overnight, 37°C, 500 rpm). After a
601 cleaning step with SP3 beads, peptides were dried, suspended in Formic Acid (FA) 0.1%,
602 DMSO 2% and injected in the mass spectrometer. Samples were analyzed on a Q Exactive HF
603 mass spectrometer coupled with a nanoRSLC Ultimate 3000 system (ThermoFisher Scientific).
604 Peptides samples were loaded on a C18 Acclaim PepMap100 trap-column 300 µm ID x 5 mm,
605 5 µm, 100Å (ThermoFisher Scientific) and separated on a C18 Acclaim Pepmap100 nano-
606 column, 50 cm x 75 µm i.d, 2 µm, 100 Å (ThermoFisher Scientific) with a 60 minutes linear

607 gradient from 3% to 90% buffer B (A: 0.1% FA in H_2O, B: 0.1% FA in ACN). The flow rate
608 was maintained at 300 nL/min and the oven temperature was kept constant at 40°C. Peptides
609 were analysed using a DDA TOP20 HCD method: MS data were acquired in a data dependent
610 strategy (DDA) selecting the fragmentation events based on the 20 most abundant precursor
611 ions in a survey scan (350-1400 Th). Resolutions of the survey and MS/MS scans were
612 respectively set at 60,000 and 15,000 at m/z 200 Th. The Ion Target Values for the survey and
613 the MS/MS scans in the Orbitrap were set to 3E6 and 1E5 respectively and the maximum
614 injection times were set to 60 ms for both MS and MS/MS scans. Parameters for acquiring
615 HCD MS/MS spectra were as follows: collision energy = 27 and isolation window = 2 m/z.
616 The precursors with unknown charge state, charge state of 1 and 8 or greater than 8 were
617 excluded. Peptides selected for MS/MS acquisition were then placed on an exclusion list for
618 30 s using the dynamic exclusion mode to limit duplicate spectra.
619
620 **Mass spectrometry analyses**
621 Each batch of experiment included TurboID and TAZ fused to TurboID samples (Table S2),
622 and csGBP-TurboID, csGBP-TurboID with VN-TAZ, csGBP-TurboID with VN-TAZ and
623 CC-14-3-3e, csGBP-TurboID with VN-TAZ and CC-TEAD2 samples (Table S3). Each
624 condition was performed in three independent biological replicates. Raw mass spectrometry
625 data were analysed using MaxQuant free software including the Andromeda search Engine
626 [46]. Using *Homo sapiens* (Swissprot) database peptide were identified. Default parameters of
627 MaxQuant were used with the following modifications: digestion by Trypsin/P and LysC,
628 lysine biotinylation as variable modification (as well as methionine oxidation and N-terminal
629 acetylation), cytosine carbamidomethylation as fixed modification, Instrument set Orbitrap
630 (with precursor tolerance 20 ppm, MS tolerance 0.5 Da), match between runs option was
631 activated, FDR 1%, label-free quantification (LFQ) and iBAQ were calculated (Tables S2 and
632 S3). Protein enrichment was calculated using the LFQ Log2 ratio and normalized on the median
633 value (Table S2 and S3). For each ratio, distribution (90%) and corresponding standard
634 deviations (SD) were calculated to define the proteins significantly enriched (ratio > confidence
635 interval defined as median ± 2 SD). Imputation of value divided by 0 (referred to infinite) has
636 been performed for confidence intervals calculation (Table S1 and S2). Subsequently, proteins
637 significantly enriched in at least 2 replicates were considered biologically relevant considering
638 biological variability and stochasticity of the MS-process and used for further analysis (Table
639 S2 and S3). Enriched proteins from the different samples were then compared with discriminate
640 proteins enriched in proximity with csGBP-TurboID individually or in proximity with VN173-

641 TAZ alone. Details about the filtering process are detailed (Fig. S5). For TAZ generic
642 candidates, protein enrichment was calculated using the LFQ Log2 ratio of TAZ-
643 TurboID/TurboID and normalized on the median value with distribution (90%) and
644 corresponding standard deviations (SD) were calculated to define the proteins significantly
645 enriched (ratio > confidence interval defined as median ± 2 SD).
646 The mass spectrometry proteomics data have been deposited to the Center for Computational
647 Mass Spectrometry repository (University of California, San Diego) via the MassIVE tool with
648 the dataset identified MassIVE MSV000095990.
649
650 **Data analysis and visualisation**
651 For proteome analysis, Perseus free software was used to generate clustering visualization
652 (PCA, [47]), based on LFQ log10 value of protein expressed after Perseus canonical filtering
653 (Reverse, Potential Contaminant, only identified by site) and replacement of missing values.
654 Functional networks of TAZ interactome were generated with STRING software [48], based
655 on 0.15 interaction score of experimental evidence and database and pathway co-occurrence.
656 Visualization of networks was built with Cytoscape free software [49]. For GO-Term
657 annotations and over-represented GO-Term related to biological process analysis was
658 performed using PANTHER [50] and represented using Prism. The selection of significant
659 GO-term was corrected by FDR<0.05, a fold enrichment higher than 10 and a raw p-
660 value>0.05. Statistical analyses were performed using one-way ANOVA (BiFC quantification,
661 siRNA effect, proliferation assay). Predictions of TAZ/1433e/SERPINB4 interaction model
662 was performed using Alphafold [37].
663
664 **BiFC and bicolor BiFC validation**
665 For transfection, 3.10^5 HEK293T cells were seeded on glass coverslips in 6-well plates and
666 incubated for 24h. Then, cells were transfected with jetPRIME (Ref 114-15, Polyplus
667 Transfection, France) following manufacturer's instructions. A total of 1 µg of plasmid DNA
668 (CC, VN and CC tagged proteins constructs including mcherry reporter to assess transfection
669 efficiency) was transfected per well. After 14h of incubation in the presence of doxycycline
670 (100 ng/mL), the cell-coated coverslip was taken and mounted carefully on a glass slide for
671 image capturing under Zeiss LSM780 confocal microscope (Carl Zeiss, Jena, Germany). All
672 samples were imaged using identical settings and were quantified as previously described [45].
673 Three biological replicates were systematically performed.
674

675 **RTqPCR and siRNA**

676 For siRNA transfection, 3.10^5 cells per ml were seeded on 6-well plates, and 10 pmol/mL of
677 total siRNA was transfected with INTERFERin (Polyplus Transfection, France) according to
678 the manufacturer's recommendations. Total RNAs were extracted using the MACHEREY-
679 NAGEL RNA extraction kit (REF 744352.4). A total of 500 ng of RNA was converted to first-
680 strand cDNA using the RevertAid First Strand cDNA Synthesis Kit (Thermo Scientific, MA,
681 USA). Real-time qPCRs were performed in 96-well plates using the IQ SYBR Green Supermix
682 (Catalog #1708880, BioRad, CA, USA). Data were quantified using ΔΔ-Ct method and were
683 normalized to GAPDH expression. siRNA and primers sequence used in the study are
684 summarized (Table S4).

685

686 **HS27A cells differentiation, Alizarin Red staining and RNAseq**

687 ***RNA samples***

688 HS27A cells differentiation protocol toward osteoblasts was adapted from the team of Dr.
689 Véronique Maguer-Satta (Cancer Research Center of Lyon - CRCL). HS27A cells were
690 cultured in human Osteoblast differentiation media (417D-250) for 15 days. Cells undergo
691 Alizarin red stain which labels calcium deposit to verify the differentiation. For staining, cells
692 were rinsed in 1X PBS and fixed with 4% PFA for 30min. This is followed by washing cells
693 with water and staining with 2% Alizarin solution (pH 4.2) for 2-3 min. RNA was extracted
694 from cells at proliferating and differentiating states using MACHEREY-NAGEL RNA
695 extraction kit (Ref 744352.4).

696 ***Construction of the libraries and sequencing***

697 Determination of RNA concentration by fluorometric assay (Qubit4.0, Thermofisher) and
698 analysis of distribution profiles of total RNA samples by capillary electrophoresis (Tapestation
699 4150, Thermofisher) were conducted by the Sequencing platform (PSI, IGFL, Lyon). The
700 quality and quantity of the triplicate samples were satisfactory for initiating library
701 construction, with no degradation of samples observed and RIN values > 8.6. mRNA capture
702 was performed using the "NEBNext® Poly(A) mRNA Magnetic Isolation Module" protocol
703 (New England Biolabs, E7490L) with a starting material of 1µg of total RNA for each sample,
704 the various steps of the protocol having been carried out according to the supplier's
705 recommendations. Libraries were constructed using the Lexogen protocol "CORALL Total
706 RNA-Seq Library Prep Kit with UDI 12 nt Set B1" protocol (Clinisciences, 118.96) according
707 to the supplier's recommendations and from 10µl of previously purified mRNA per sample. 16

708 cycles of PCR amplification were performed to finalize the construction of indexed library.
709 The libraries were quantified (Qubit4.0, Thermofisher) and qualified (Tapestation 4150,
710 Thermofisher). Sequencing was performed on the Illumina NextSeq 500 platform using Mid
711 Output reagents with the following parameters: PE 2x81bp and 6bp index i7. A total of
712 194,006,581 reads were generated (Table S3).
713
714 ***Bioinformatics analyses***
715 Reads were mapped onto the human genome using a local pipeline derived from the one
716 supported by Lexogen (https://www.lexogen.com/corall-data-analysis/). Lexogen has made
717 their pipeline available on the Lexogen's Kangooroo app webpage
718 (https://kangooroo.com/home). In brief, UMI were first trimmed with the program umi_tools
719 extract (version 1.1.2, [51]). Adapter sequences were then removed using the Cutadapt package
720 (version 3.5, [52]) and reads quality control was performed using FastQC (version 0.11.8;
721 https://www.bioinformatics.babraham.ac.uk/projects/fastqc/). Read mapping was achieved
722 with STAR (Spliced Transcripts Alignment to a Reference, version 2.6.1a, [53]) using the
723 Homo sapiens GRCh38 genome reference (Ensembl, release 109). UMI deduplication was
724 conducted with the program umi_tools dedup (version 1.1.2, [51]) enabling the accurate
725 bioinformatic identification of PCR duplicates. The mapped reads were then quantified by Mix²
726 (version 1.4.0.1, [54]), allowing to generate a count table per sample. Differential gene
727 expression analysis was performed with DESeq2 [55] using a custom R script available on the
728 following GitLab repository: https://gitbio.ens-lyon.fr/igfl/merabet/HS27ADiff. A Docker
729 image is also provided to reproduce the results of the analysis.
730
731 **xCELLigence Assays**
732 The xCELLigence system (ACEA Biosciences Inc., San Diego, CA, USA), which records
733 cellular events in real time by measuring electrical impedance across microelectrodes
734 integrated on the bottom of culture plates (E-plates), was utilized in proliferation experiments.
735 First, HS27A cell culture media were added to each well of 16-well E-plates (ACEA
736 Biosciences Inc., San Diego, CA, USA) to measure background impedance. Then, 10.10^3 of
737 HS27A cells were transfected with a mixture of control, 14-3-3e, TAZ, SERPINB4 siRNAs at
738 10 pmol/mL using INTERFERin (Polyplus Transfection, France) according to the
739 manufacturer's protocol. Transfected cells were directly seeded on E-plates ($5 .10^5$ cells/well),
740 and the impedance was measured every 15 min for 96 h. The impedance signal was
741 proportional to the number of cells proliferating in each well and was displayed as cell index.

742 Data were analyzed with the RTCA Software 2.0 and were presented as mean +/− SEM of
743 three experiments performed in triplicate.
744
745 **Figure legends**
746 **Figure 1: Capturing the generic interactome of TAZ-TurboID in HEK-293T cells. (A)**
747 Schematic representation of the capture of TAZ-TurboID interactome. The addition of Biotin
748 leads to the labeling of proteins in proximity to the bait protein construct. Biotinylated proteins
749 are affinity purified with streptavidin-coupled beads and analyzed by liquid chromatography
750 coupled to tandem mass spectrometry (LC-MS/MS). **(B)** Validation of the specific
751 biotinylating activity of TAZ-TurboID when compared to TurboID alone by
752 immunofluorescence in HEK293T cells. Biotinylation was revealed with streptavidin (SA)
753 coupled to the 555 dyes (red). The expression of each construct was confirmed with an
754 immunostaining against the HA tag present in each construct (gray). Dapi (blue) stains for
755 nuclei. Scale bar = 20 µm. **(C)** Western blot analysis of biotin labeling by TurboID or TAZ-
756 TurboID. The input and affinity purified (AP) biotinylated proteins from samples expressing
757 each construct were analyzed via western blotting after biotin incubation (10 minutes). Samples
758 were probed by streptavidin conjugate, HA and Histone 3 (H3) antibodies. The band
759 corresponding to TurboID or TAZ-TurboID is indicated with anti-HA. **(D)** GO term analysis
760 of the TAZ-TurboID interactome compared to the known interactions of TAZ in the literature.
761 The 177 novel interactions captured in this study have several GO term enrichments directly
762 (box) or indirectly related to the Hippo signaling pathway. **(E-E')** Principle of BiFC with Venus
763 and Cerulean derived fragments. The N-terminal fragment of Venus (VN) can complement
764 with the C-terminal fragment of Cerulean (CC) and provide a Venus-like fluorescence signal.
765 **(F)** Illustrative confocal acquisitions of BiFC between VN-Taz and new candidate partners
766 fused to CC, as indicated. Hoechst stains for nuclei in live HEK293T cells (blue). Scale
767 bar = 20 µm.
768
769 **Figure 2: Establishing Bi-nano-ID experimental parameters in HEK293T cells. (A)**
770 Principle of Bi-nano-ID. BiFC resulting from the complementation between the VN and CC
771 fragment is recognized by a GFP nanobody (csGBP) coupled to the TurboID enzyme. The
772 addition of biotin allows the biotinylation of surrounding partners, which can then be purified
773 by affinity purification (AP) and analyzed by mass spectrometry (LC-MS/MS). **(B)**
774 Simultaneous visualization of the interaction between a novel candidate partner (gray ball) and
775 the bait dimeric complex. The superposition of Venus- (green) and Cerulean-like (blue)

776 fluorescent signals in the cell is indicative of co-localized interactions, therefore of possible
777 trimeric complex assembly. **(C-D)** Validation of the specificity of Bi-nano-ID by
778 immunofluorescence. Biotinylation is revealed with streptavidin (SA) coupled to 555 dyes
779 (red). Interaction between the fusion TAZ and 14-3-3e (C) or TEAD2 (D) proteins is revealed
780 by BiFC (green). Dapi stains for nuclei (blue). Enlargements highlight the specific
781 colocalization of red and green signals in the cytoplasm or the nucleus for TAZ/14-3-3e and
782 TAZ/TEAD2 complexes, respectively. Scale bar = 20 µm. **(E)** Western blot of affinity purified
783 biotinylated proteins from samples expressing dsGBP-TurboID individually or in combination
784 with VN173-TAZ, and/or CC-14-3-3e or CC/TEAD2. Experiment was performed after
785 different biotin (50 µM) incubation timepoints (10, 90, 180, 240 minutes), as indicated.
786 Samples were probes by streptavidin conjugate (to reveal biotinylated proteins) and GFP (to
787 reveal the VN and CC fusion constructs). Colored arrowheads depict sizes corresponding to
788 VN-TAZ (blue arrowhead), CC-14-3-3e (magenta arrowhead) and CC-TEAD2 (orange
789 arrowhead). Note that non-specific bands with the nanobody alone are present at the size of
790 VN-TAZ and CC-TEAD2. These bands were taken into account for the quantification of the
791 biotinylation activity of the nanobody with VN-TAZ (upper band) and CC-TEAD2 (lower
792 band). **(E')** Quantification of the intensity of the biotinylation bands in the different conditions
793 at 180min biotin incubation time, as indicated. Quantification was obtained from three
794 biological replicates. Statistical tests were performed with one-way ANOVA (*$p < 0.05$,
795 ****$p < 0.0001$).
796
797 **Figure 3: TAZ/14-3-3e and TAZ/TEAD2 interactome clustering. (A)** Venn diagrams
798 showing common and specific interactions between TAZ-TurboID, TAZ/14-3-3e and
799 TAZ/TEAD2 interactomes. **(B-B')** Specific interactions and GO term enrichment for TAZ/14-
800 3-3e interactome. Light-to-dark pink gradient illustrates low-to-high protein enrichment,
801 respectively (as deduced from the LFQ value of mass spectrometry data, see also Table S2).
802 Cytoplasmic proteins are surrounded (black circle). **(C-C')** Specific interactions and GO term
803 enrichment for TAZ/TEAD2-interactome. Light-to-dark orange gradient illustrates low-to-
804 high protein enrichment, respectively (as deduced from the LFQ value of mass spectrometry
805 data, see also Table S2). Nuclear proteins are surrounded (black circle).
806
807 **Figure 4. Role of SERPINB3 and SERPINB4 in TAZ/14-3-3e-dependent proliferation of**
808 **HS27A mesenchymal stem cells. (A)** HS27A cells differentiate into osteoblast and are stained
809 with alizarin (red) after 15 days of culture in an osteoblast differentiation medium. **(A')**

810 Statistical quantification of the HS27A cell alizarin staining at day 3, 7 and 15 of culture.
811 Statistical tests were performed with one-way ANOVA (****$p < 0.0001$). **(B)** Distribution as
812 a volcano plot of up- (Log2FC>0.5 and Log10*pvalue*>0,8) or down- (Log2FC<-0.5 and
813 Log10*pvalue*>-0,8) regulated genes during the differentiation of HS27A cells (as deduced from
814 RNA-seq. experiments performed at day 1 and day 15). **(C)** String interactome for SERPINB4
815 (based on 0.15 interaction score of experimental evidence and database and pathway co-
816 occurrence). **(D)** Quantification with xCELLigence assays of HS27A cells transfected with the
817 different siRNAs, as indicated. siC = siRNA control (see also Materials and Methods).
818 Measures were performed at different time points post-transfection and resulted from three
819 independent biological replicates. Two-way ANOVA with Tukey's multiple comparisons;
820 * $p < 0.05$ and **** $p < 0.0001$.
821
822 **Figure 5: TAZ, 14-3-3e and SERPINB4 establish cooperative protein-protein interactions**
823 **in living HEK293T cells. (A)** Scheme of bicolor BiFC illustrating Venus- and Cerulean-like
824 signals resulting from TAZ/14-3-3e and 14-3-3e/SERPINB4 interactions, respectively. **(A')**
825 Illustrative confocal acquisition showing the simultaneous interaction profile of TAZ/14-3-3e
826 (green) and 14-3-3e/SERPINB4 (blue) in living HEK293T cells. **(B)** Scheme of bicolor BiFC
827 illustrating Venus- and Cerulean-like signals resulting from TAZ/SERPINB4 and 14-3-
828 3e/SERPINB4 interactions, respectively. **(B')** Illustrative confocal acquisition showing the
829 simultaneous interaction profile of TAZ/SERPINB4 (green) and 14-3-3e/SERPINB4 (blue) in
830 living HEK293T cells. **(C)** Scheme of BiFC performed between 14-3-3e and SERPINB4
831 (green) when co-expressing or not HA-tagged TAZ. **(C')** Illustrative confocal acquisition of
832 BiFC (green) between 14-3-3e and SERPINB4 without (first column) or with HA-TAZ
833 overexpression, as indicated. HA-TAZ was revealed with an anti-HA antibody (gray) and
834 mCherry (red) stains for transfection efficiency. **(C'')** Quantification of the BiFC (normalized
835 over transfection efficiency) between 14-3-3e and SERPINB4 in the absence (first column) or
836 presence (second column) of HA-TAZ.
837 **(D)** Scheme of BiFC performed between TAZ and SERPINB4 (green) when affecting or not
838 the expression of endogenous *14-3-3e*. **(D')** Illustrative confocal acquisition of BiFC between
839 TAZ and SERPINB4 (green) in the siRNA control (ctrl) condition or when co-transfecting
840 siRNA targeting endogenous *14-3-3e*, as indicated. Merge with Hoechst (blue) and mCherry
841 (red) stains for nuclei and transfection efficiency, respectively. **(D'')** Quantification of the
842 BiFC (normalized over transfection efficiency) between TAZ and SERPINB4 with no siRNA
843 (first column), control siRNA (second column) or siRNA against *14-3-3e* (third column).

844 Statistical tests were performed with one-way ANOVA from three biological replicates (ns:
845 non-significant, ***$p < 0.001$, **$p < 0.01$). Scale bar = 20 µm.
846
847 **Figure 6: The Glu309 residue of TAZ is critical for recruiting SERPINB4 specifically in**
848 **the presence of 14-3-3e**
849 **(A)** Scheme of bicolor BiFC with the mutated TAZ^{E309A} construct and illustrating the confocal
850 observations in A'. **(A')** Illustrative confocal acquisition showing the loss of BiFC between
851 mutated TAZ^{E309A} and SERPINB4 (green) and the decreased BiFC between SERPINB4 and
852 14-3-3e (blue) in living HEK293T cells. mCherry (red) stains for transfection efficiency in the
853 merge picture. **(A'')** Quantification of the BiFC (normalized over transfection efficiency)
854 between wild type or mutated TAZ and SERPINB4 (first two columns), and between
855 SERPINB4 and 14-3-3e with wild type or mutated TAZ (last two columns) co-transfection
856 conditions. **(B)** Scheme of BiFC performed between 14-3-3e and SERPINB4 (green) when co-
857 expressing or not the HA-tagged mutated form of TAZ. **(B')** Illustrative confocal acquisition
858 of BiFC between 14-3-3e and SERPINB4 without (first column) or with (second column) co-
859 expression of mutated HA-TAZ^{E309A}, as indicated. Mutated HA-TAZ^{E309A} was revealed with
860 an anti-HA antibody (gray). mCherry (red) stains for transfection efficiency. **(B'')**
861 Quantification of BiFC (normalized over transfection efficiency) between 14-3-3e and
862 SERPINB4 in the absence (first column) or presence of wild type HA-TAZ (second column)
863 or mutated HA-TAZ^{E309A} (third column). **(C)** Scheme of BiFC performed between mutated
864 TAZ^{E309A} and SERPINB4 (green) when affecting or not the expression of endogenous *14-3-*
865 *3e*. **(C')** Illustrative confocal acquisition of BiFC between mutated TAZ^{E309A} and SERPINB4
866 (green) in the siRNA control (ctrl) condition or when co-transfecting siRNA targeting
867 endogenous *14-3-3e*, as indicated. Merge with Hoechst (blue) and mCherry (green) stains for
868 nuclei and transfection efficiency, respectively. **(C'')** Quantification of the BiFC (normalized
869 over transfection efficiency) between mutated TAZ^{E309A} and SERPINB4 with no siRNA (first
870 column), control siRNA (second column) or siRNA against *14-3-3e* (third column). Statistical
871 tests were performed with one-way ANOVA from three biological replicates (ns: non-
872 significant, **$p < 0.01$, ****$p < 0.0001$). Scale bar = 20 µm.
873
874 **Figure 7. A specific interaction mode underlies the formation of TAZ/14-3-3e/SERPINB4**
875 **trimeric complexes.** The Glu309 of TAZ is a unique contact residue for SERPINB4, being
876 responsible of the formation of a cooperative trimeric complex with 14-3-3e. The trimeric
877 TAZ/14-3-3e/SERPINB4 complex relies on specific interaction interfaces that are not used in

878 the dimeric complexes. Accordingly, the TAZ^{E309A} mutated form can interact with SERPINB4
879 and the corresponding dimeric complex is insensitive to the absence of 14-3-3e. Thus, the
880 formation of trimeric TAZ/14-3-3e/SERPINB4 complexes relies on strong protein interaction
881 remodeling when compared to the dimeric TAZ/14-3-3e or TAZ/SERPINB4 complexes. This
882 remodeling could have incidence on the overall protein complex stability and proliferation
883 activity. Sites of contact with 14-3-3e and SERPINB4 are highlighted in TAZ for the dimeric
884 and trimeric complexes (as deduced from AlphaFold and Endscript predictions).
885
886 **Supplementary Figures**
887 **Supplementary Figure 1. Biotinylation activity and interactome properties of TAZ-**
888 **TurboID in HEK293T cells. (A)** Quantification of the SA-555 immunostaining in HEK293T
889 cells expressing TurboID or TAZ-TurboID, as indicated. Quantification was normalized over
890 HA-staining. **(B)** Quantification of the intensity of bands revealed with the streptavidin staining
891 for TurboID and TAZ-TurboID, as indicated. Quantification was normalized over HA-staining
892 from the input. **(C)** Principal component analysis of TurboID and TAZ-TurboID replicates. **(D)**
893 Venn diagram for TAZ-TurboID specific interactions (after filtering against TurboID) captured
894 with the three biological replicates (R1-R3). **(E)** Go term analysis of the 66 common
895 interactions between TAZ-TurboID and the known interactions of TAZ in the literature, and of
896 the remaining 275 known interactions not captured in this study. **(F)** Illustrative confocal
897 acquisitions of BiFC between VN-TAZ and new candidate partners already known in the
898 literature and fused to CC, as indicated. Hoechst stains for nuclei in live HEK293T cells (blue).
899 Scale bar = 20 µm.
900
901 **Supplementary Figure 2. Comparison between VN173 and VN155 for doing Bi-nano-ID.**
902 **(A)** Scheme of the complementation between VN155 or VN173 from Venus and CC from
903 Cerulean. The two complementation systems produce a Venus-like signal. **(B-B')** Comparison
904 of BiFC performed with VN173-TAZ (B) or VN155-TAZ (B'). BiFC was performed with CC-
905 14-3-3e or CC-TEAD2 in live HEK293T cells. Hoechst stains for nuclei (blue) and mCherry
906 (mCh) for transfection efficiency (red). **B''** Quantification of BiFC obtained with VN173-TAZ
907 or VN155-TAZ. BiFC was normalized over transfection efficiency in each condition.
908 Quantification was deduced from at least three biological replicates. Statistical tests were
909 performed with one-way ANOVA (****$p < 0.0001$). **(C)** Validation of the weak biotinylation
910 activity of csGBP-TurboID when doing BiFC with VN155-TAZ. Biotinylation is revealed with
911 streptavidin (SA) coupled to the 555 dye (red). Interaction between the fusion TAZ and 14-3-

912 3e or TEAD2 is revealed by BiFC (green). Dapi stains for nuclei (blue). Scale bar = 20 µm.
913 **(C')** Quantification of the biotinylation signal for each condition, as indicated. Quantification
914 was obtained from three biological replicates. Statistical tests were performed with one-way
915 ANOVA (****$p < 0.0001$).
916
917 **Supplementary Figure 3. Specificity of the csGBP nanobody for the BiFC. (A)** Fluorescent
918 immunostaining with SA-555 (red) and anti-GFP (green) recognizing the VN and CC fragment
919 with single construct transfection, as indicated. DAPI (blue) stains for nuclei. **(A')**
920 Quantification of the biotinylation signal when compared to signals obtained with BiFC
921 complexes. Quantification was obtained from three biological replicates. Statistical tests were
922 performed with one-way ANOVA (****$p < 0.0001$).
923
924 **Supplementary Figure 4. Western blots of biotinylated proteins extracted from**
925 **HEK293T cells upon transfection with the different constructs, as indicated. (A)** Input
926 fraction of extracted proteins revealed on the gel probed by streptavidin, GFP and H3
927 antibodies. Colored arrowheads indicate the band corresponding to VN173-TAZ (blue
928 arrowhead), CC-14-3-3e (magenta arrowhead) and CC-TEAD2 (orange arrowhead). **(A')**
929 Histogram showing the quantification of the biotinylation bands in each condition, as indicated.
930 The quantification was deduced by subtracting the AP band with the corresponding input band.
931 It also took into account the non-specific AP bands of the nanobody for quantifying
932 biotinylation of VN-TAZ and CC-TEAD2 (see Fig. 2). Statistical tests were performed with
933 one-way ANOVA from three biological replicates (****$p < 0.0001$, *$p < 0.05$).
934
935 **Supplementary Figure 5. Filtering steps for identifying TAZ/14-3-3e and TAZ/TEAD2**
936 **interactomes.** Filter 1 was applied to remove BiFC interaction candidates that were also found
937 with dsGBP-TurboID alone (comparing BiFC+csGBP-TurboID to csGBP-TurboID condition
938 in each replicate). Filter 2 identified interactions obtained with VN173-TAZ alone when
939 compared to the dsGBP-TurboID condition in each replicate. Filter 3 identified BiFC-specific
940 interactions when removing interactions found with csGBP-TurboID alone (filter 1) and VN-
941 TAZ alone (filter 2). Only interactions found in 2 or 3 replicates were considered. This filtering
942 was applied for TAZ/14-3-3e (upper panel) and TAZ/TEAD2 (lower panel) complexes, leading
943 to the identification of 98 and 42 interactions, respectively.
944

945 **Supplementary Figure 6. Molecular clustering of TAZ-TurboID, TAZ/14-3-3e and**
946 **TAZ/TEAD2 interactomes.**
947
948 **Supplementary Figure 7. Functional clustering of TAZ-TurboID, TAZ/14-3-3e and**
949 **TAZ/TEAD2 interactomes.** The clustering was based on GO terms that were 10 times
950 enriched at the minimum. Specific TAZ/14-3-3e and TAZ/TEAD2 Go term enrichments are
951 shown in the Fig. 3.
952
953 **Supplementary Figure 8. Alignment of SERPINB3 and SERPINB4 protein sequences.**
954 Alignment was obtained by using the CLUSTALW web tool from PRABI
955 (https://prabi.ibcp.fr/htm/site/web/app.php/home).
956
957 **Supplementary Figure 9. Effects of siRNAs. (A)** Effect of siRNAs targeting *SERPINB3* and
958 *SERPINB4* on endogenous *SERPINB3* in HS27A cells. **(B)** Effect of siRNAs targeting
959 *SERPINB3* and *SERPINB4* on endogenous *SERPINB4* in HS27A cells. **(C)** Effect of siRNAs
960 targeting *14-3-3* on endogenous *SERPINB4* expression in HS27A cells. **(D)** Effect of siRNAs
961 targeting *TAZ* on endogenous *SERPINB4* expression in HS27A cells. **(E)** Effect of siRNAs
962 targeting *14-3-3* on endogenous *SERPINB4* expression in HEK293T cells. **(F-F'')** Effects of
963 siRNAs targeting *TAZ* (F), *14-3-3e* (F') or *SERPINB3/B4* (F'') on endogenous *TAZ* expression
964 in HS27A cells. **(G)** Effects of siRNAs targeting *14-3-3e* on endogenous *TAZ* expression in
965 HEK293T cells. **(H-H'')** Effects of siRNAs targeting *TAZ* (H), *14-3-3e* (H') or *SERPINB3/B4*
966 (H'') on endogenous *14-3-3e* expression in HS27A cells. **(I)** Effects of siRNAs targeting *14-*
967 *3-3e* on endogenous *14-3-3e* expression in HEK293T cells. Graphs result from the
968 quantification of RTqPCR from three biological replicates in each condition. Statistical tests
969 were performed with one-way ANOVA (ns: non-significant, $^{**}p < 0.01$, $^{****}p < 0.0001$).
970 Note that *SERPINB3* and *SERPINB4* are 98% identical at the nucleotide sequence level.
971
972 **Supplementary Figure 10. Structure and interaction predictions for TAZ, 14-3-3e,**
973 **SERPINB3 and SERPINB4. (A)** AlphaFold multimer prediction of TAZ/14-3-3e/SERPINB3
974 trimeric protein complex. **(B)** AlphaFold multimer prediction of TAZ/14-3-3e/SERPINB4
975 trimeric protein complex. Enlargements highlight the disordered C-terminal region of TAZ in
976 contact with SERPINB3 (A) or SERPINB4 (B) and 14-3-3e (highlighted with a light-yellow
977 box). **(C)** Enlargement at the level of the Glu309 residue of TAZ that makes contacts with two
978 Lys residues of SERPINB4. Among other residues in contact with 14-3-3e in the same region,

979 the residue Arg308 of TAZ interacts with the residue Asp234 of 14-3-3e. **(D)** Prediction of
980 disordered regions (red line above the gray line), ordered domain (blue box), short linear
981 interaction motifs (violet boxes) and LATS1-phosphorylation sites in TAZ protein sequence.
982 Adapted from ELM (http://elm.eu.org/search.html) and IUPred2A (https://iupred2a.elte.hu/).
983 **(E-E')** Quantification of wild type or mutated TAZ expression in HEK293T cells. VN-fusion
984 constructs were revealed with anti-GFP (green). Dapi stains for nuclei. Statistical tests were
985 performed with one-way ANOVA (****$p < 0.0001$).
986
987 **Supplementary Figure 11. Endscript2 analyses of interaction contacts predicted in the**
988 **TAZ/14-3-3-3e/SERPINB3 (A) and TAZ/14-3-3e/SERPINB4 (B) complexes.** The
989 sequences of TAZ (Chain A) 14-3-3e (chain B) and SERPINB3/4 (chain C) are presented from
990 top to bottom. They are adorned with secondary structure elements, alpha-helices being
991 represented by squiggles and beta-strands by arrows. Accessibility bar (acc, blue accessible,
992 cyan intermediate, white buried) hydropathy bar (hyd, cyan hydrophylic, pink hydrophobic)
993 and intermolecular contact letters (A to C refers to the chain of the residue contacted; a red
994 letter indicates a contact distance < 3.2 Å and a black letter a contact distance in the range 3.2-
995 3.7 Å) are written below the sequences.
996
997 **Supplementary Figure 12. AlphaFold prediction (A) and Endscript2 annotations (B) of**
998 **TAZ/SERPINB4 dimeric protein complex.**
999
1000 **Supplementary Figure 13. AlphaFold prediction (A) and Endscript2 annotations (B) of**
1001 **TAZ/14-3-3e dimeric protein complex.**
1002
1003 **Supplementary Figure 14. AlphaFold prediction (A) and Endscript2 annotations (B) of**
1004 **14-3-3e/SERPINB4 dimeric protein complex.**
1005
1006 **Supplementary Tables**
1007 **Supplementary Table 1. Mass spectrometry data and GO term enrichment for TAZ-**
1008 **TurboID**
1009
1010 **Supplementary Table 2. Mass spectrometry data and GO term enrichment for TAZ/14-**
1011 **3-3e and TAZ/TEAD2 complexes**
1012

1013 **Supplementary Table 3. RNA-seq data of HS27A cells.**
1014
1015 **Supplementary Table 4. Sequences of oligonucleotides and primers used in this study for**
1016 **cloning and RTqPCRs**
1017
1018 **Authors contribution**
1019 S.M. designed the study. N.H.S. performed the experiments and acquired the data. J.C. and
1020 N.H.S., with the support of S.M. and F.D., were responsible of proteomics data analyses. N.H.S
1021 and L.G. analyzed the RNA-seq data. Y.J. was responsible for the cytoscape network
1022 illustration. S.M. and N.H.S. wrote the paper and all authors amended it.
1023
1024 **Acknowledgments**
1025 We are beyond grateful for the help of Christelle Forcet in performing the proliferation assay
1026 and support at the experimental level. We thank also Benjamin Gillet, Sandrine Hughes and
1027 Julien Dellinger for the RNA-seq preparation and valuable help in the transcriptomic analyses.
1028 We thank Adeline PAGE from the Protein Science Facility at the SFR bioscience
1029 (UAR3444/CNRS, US8/Inserm, ENS de Lyon) for Mass spectrometry analyses. We are very
1030 grateful for the help provided by Sylvain Lefort and the team of Dr. Veronique Maguer-Satta
1031 (CRCL) for HS27A line and culturing tips. We thank Alain Guignandon and Daniel Bouvard
1032 for their valuable inputs in the project. We thank Julien Béthune for careful reading of the
1033 manuscript and helpful comments. This project was supported by Ambition Pack from the
1034 Region Rhone Alpes and the Foundation of Medical Research (FRM #FDT202304016377, 4th
1035 year grant for N.H.S).
1036
1037 **Conflict of interest**
1038 Authors declare no conflict of interest.
1039
1040 **References**
1041 1. Holguin-Cruz JA, Foster LJ, G.J. Where protein structure and cell diversity meet.
1042 *Trends Cell Biol.* **2022**, *Dec;32*, 996–1007, doi:10.1016/j.tcb.2022.04.004.
1043 2. Schaefer MH, Lopes TJ, Mah N, Shoemaker JE, Matsuoka Y, Fontaine JF, Louis-
1044 Jeune C, Eisfeld AJ, Neumann G, Perez-Iratxeta C, Kawaoka Y, Kitano H, A.-N.M.
1045 Adding protein context to the human protein-protein interaction network to reveal
1046 meaningful interactions. *PLoS Comput Biol.* **2013**, *9(1)*,

1047 doi:10.1371/journal.pcbi.1002860.
1048 3. Liu X, Abad L, Chatterjee L, Cristea IM, V.M. Mapping protein-protein interactions
1049 by mass spectrometry. *Mass Spectrom Rev.* **2024**, *May 14*, doi:10.1002/mas.21887.
1050 4. Branon TC, Bosch JA, Sanchez AD, Udeshi ND, Svinkina T, Carr SA, Feldman JL,
1051 Perrimon N, T.A. Efficient proximity labeling in living cells and organisms with
1052 TurboID. *Nat Biotechnol.* **2018**, *Oct 36*, 880–887, doi:10.1038/nbt.4201.
1053 5. Cho KF, Branon TC, Rajeev S, Svinkina T, Udeshi ND, Thoudam T, Kwak C, Rhee
1054 HW, Lee IK, Carr SA, T.A. Split-TurboID enables contact-dependent proximity
1055 labeling in cells. *Proc Natl Acad Sci U S A.* **2020**, *Jun 2*, 12143–12154,
1056 doi:10.1073/pnas.1919528117.
1057 6. Takano T, Wallace JT, Baldwin KT, Purkey AM, Uezu A, Courtland JL, Soderblom
1058 EJ, Shimogori T, Maness PF, Eroglu C, S.S. Chemico-genetic discovery of astrocytic
1059 control of inhibition in vivo. *Nature* **2020**, *Dec;588*, 296–3027837,
1060 doi:10.1038/s41586-020-2926-0.
1061 7. Takano T, S.S. Tripartite synaptomics: Cell-surface proximity labeling in vivo.
1062 *Neurosci Res.* **2021**, *Dec*, 14–21, doi:10.1016/j.neures.2021.05.002.
1063 8. Barroso-Gomila O, Trulsson F, Muratore V, Canosa I, Merino-Cacho L, Cortazar AR,
1064 Pérez C, Azkargorta M, Iloro I, Carracedo A, Aransay AM, Elortza F, Mayor U,
1065 Vertegaal ACO, Barrio R, S.J. Identification of proximal SUMO-dependent interactors
1066 using SUMO-ID. *Nat. Commun.* **2021**, *12*, 6671, doi:10.1038/s41467-021-26807-6.
1067 9. Panciera T, Azzolin L, Cordenonsi M, P.S. Mechanobiology of YAP and TAZ in
1068 physiology and disease. *Nat Rev Mol Cell Biol.* **2017**, *Dec;18*, 758–770,
1069 doi:10.1038/nrm.2017.87.
1070 10. Fu M, Hu Y, Lan T, Guan KL, Luo T, L.M. The Hippo signalling pathway and its
1071 implications in human health and diseases. *Signal Transduct Target Ther.* **2022**, *Nov 8*,
1072 376, doi:10.1038/s41392-023-01682-3.
1073 11. Yang W, Han W, Qin A, Wang Z, Xu J, Q.Y. The emerging role of Hippo signaling
1074 pathway in regulating osteoclast formation. *J Cell Physiol.* **2018**, *Jun;233*, 4606–4617,
1075 doi:10.1002/jcp.26372.
1076 12. Kovar H, Bierbaumer L, R.-S.B. The YAP/TAZ Pathway in Osteogenesis and Bone
1077 Sarcoma Pathogenesis. *Cells* **2020**, *Apr 15;9*, 972, doi:10.3390/cells9040972.
1078 13. Ou WB, Lundberg MZ, Zhu S, Bahri N, Kyriazoglou A, Xu L, Chen T, Mariño-
1079 Enriquez A, F.J. YWHAE-NUTM2 oncoprotein regulates proliferation and cyclin D1
1080 via RAF/MAPK and Hippo pathways. *Oncogenesis* **2021**, *May 4;10*, 37,

1081 doi:10.1038/s41389-021-00327-w.
1082 14. Wang Y, Li F, Ma D, Gao Y, Li R, G.Y. MicroRNA-608 sensitizes non-small cell lung
1083 cancer cells to cisplatin by targeting TEAD2. *Mol Med Rep.* **2019**, *Oct;20*, 3519–3526,
1084 doi:10.3892/mmr.2019.10616.
1085 15. Joo JS, Cho SY, Rou WS, Kim JS, Kang SH, Lee ES, Moon HS, Kim SH, Sung JK,
1086 Kwon IS, Eun HS, L.B. TEAD2 as a novel prognostic factor for hepatocellular
1087 carcinoma. *Oncol Rep.* **2020**, *Jun;43*, 1785–1796, doi:10.3892/or.2020.7578.
1088 16. Huttlin EL, Ting L, Bruckner RJ, Gebreab F, Gygi MP, Szpyt J, Tam S, Zarraga G,
1089 Colby G, Baltier K, Dong R, Guarani V, Vaites LP, Ordureau A, Rad R, Erickson BK,
1090 Wühr M, Chick J, Zhai B, Kolippakkam D, Mintseris J, Obar RA, Harris T, Artavanis-
1091 Tsakonas S, G.S. The BioPlex Network: A Systematic Exploration of the Human
1092 Interactome. *Cell* **2015**, *Jul 16;162*, 425–440, doi:10.1016/j.cell.2015.06.043.
1093 17. Ren H, Ou Q, Pu Q, Lou Y, Yang X, Han Y, L.S. Comprehensive Review on
1094 Bimolecular Fluorescence Complementation and Its Application in Deciphering
1095 Protein-Protein Interactions in Cell Signaling Pathways. *Biomolecules.* **2024**, *Jul 17*,
1096 859, doi:10.3390/biom14070859.
1097 18. Ariotti, N.; Rae, J.; Giles, N.; Martel, N.; Sierecki, E.; Gambin, Y.; Hall, T.E.; Parton,
1098 R.G. Ultrastructural localisation of protein interactions using conditionally stable
1099 nanobodies. *PLoS Biol.* **2018**, *16*, doi:10.1371/journal.pbio.2005473.
1100 19. Croucher DR, Iconomou M, Hastings JF, Kennedy SP, Han JZ, Shearer RF, McKenna
1101 J, Wan A, Lau J, Aparicio S, S.D. Bimolecular complementation affinity purification
1102 (BiCAP) reveals dimer-specific protein interactions for ERBB2 dimers. *Sci Signal.*
1103 **2016**, *Jul 12;9*, doi:10.1126/scisignal.aaf0793.
1104 20. Zeng L, Wang WH, Arrington J, Shao G, Geahlen RL, Hu CD, T.W. Identification of
1105 Upstream Kinases by Fluorescence Complementation Mass Spectrometry. *ACS Cent*
1106 *Sci.* **2017**, *Oct 25;3*, 1078–1085.
1107 21. Hu, C.-D.; Kerppola, T.K. Simultaneous visualization of multiple protein interactions
1108 in living cells using multicolor fluorescence complementation analysis. *Nat.*
1109 *Biotechnol.* **2003**, *21*, 539–45, doi:10.1038/nbt816.
1110 22. Kerppola, T.K. Multicolor bimolecular fluorescence complementation (BiFC) analysis
1111 of protein interactions with alternative partners. *Cold Spring Harb. Protoc.* **2013**,
1112 *2013*, 798–803, doi:10.1101/pdb.top077164.
1113 23. Nagai, T.; Ibata, K.; Park, E.S.; Kubota, M.; Mikoshiba, K.; Miyawaki, A. A variant of
1114 yellow fluorescent protein with fast and efficient maturation for cell-biological

1115 applications. *Nat. Biotechnol.* **2002**, *20*, 87–90, doi:10.1038/nbt0102-87.
1116 24. Rizzo, M. a; Springer, G.H.; Granada, B.; Piston, D.W. An improved cyan fluorescent
1117 protein variant useful for FRET. *Nat. Biotechnol.* **2004**, *22*, 445–9,
1118 doi:10.1038/nbt945.
1119 25. Abenza JF, Rossetti L, Mouelhi M, Burgués J, Andreu I, Kennedy K, Roca-Cusachs P,
1120 Marco S, García-Ojalvo J, T.X. Mechanical control of the mammalian circadian clock
1121 via YAP/TAZ and TEAD. *J Cell Biol.* **2023**, *Sep 4;222*, e202209120.,
1122 doi:e202209120.
1123 26. Shen H, Huang X, Zhao Y, Wu D, Xue K, Yao J, Wang Y, Tang N, Q.Y. The Hippo
1124 pathway links adipocyte plasticity to adipose tissue fibrosis. *Nat Commun.* **2022**, *Oct*
1125 *13;13*, 6030, doi:10.1038/s41467-022-33800-0.
1126 27. Yuan Y, Park J, Feng A, Awasthi P, Wang Z, Chen Q, I.-B.R. YAP1/TAZ-TEAD
1127 transcriptional networks maintain skin homeostasis by regulating cell proliferation and
1128 limiting KLF4 activity. *Nat Commun.* **2020**, *Mar 19;11*, 1472, doi:10.1038/s41467-
1129 020-15301-0.
1130 28. Du Z, Shi X, G.A. lncRNA H19 facilitates the proliferation and differentiation of
1131 human dental pulp stem cells via EZH2-dependent LATS1 methylation. *Mol Ther*
1132 *Nucleic Acids.* **2021**, *Apr 24*, 116–126, doi:10.1016/j.omtn.2021.04.017.
1133 29. Driskill JH, P.D. Control of stem cell renewal and fate by YAP and TAZ. *Nat Rev Mol*
1134 *Cell Biol.* **2023**, *Dec;24*, 895–911, doi:10.1038/s41580-023-00644-5.
1135 30. Luo J, L.P. Context-dependent transcriptional regulations of YAP/TAZ in stem cell
1136 and differentiation. *Stem Cell Res Ther.* **2022**, *Jan 10;13(*, doi:10.1186/s13287-021-
1137 02686-y.
1138 31. Roecklein BA, T.-S.B. Functionally distinct human marrow stromal cell lines
1139 immortalized by transduction with the human papilloma virus E6/E7 genes. *Blood*
1140 **1995**, *Feb 15;85*, 997–1005.
1141 32. Liu B, Wu S, Han L, Z.C. β-catenin signaling induces the osteoblastogenic
1142 differentiation of human pre-osteoblastic and bone marrow stromal cells mainly
1143 through the upregulation of osterix expression. *Int J Mol Med.* **2015**, *Dec;36*, 1572–82,
1144 doi:10.3892/ijmm.
1145 33. Cagnin S, Pontisso P, M.A. SerpinB3: A Multifaceted Player in Health and Disease-
1146 Review and Future Perspectives. *Cancers (Basel).* **2024**, *Jul 18;16*,
1147 doi:10.3390/cancers16142579.
1148 34. Sun Y, Sheshadri N, Z.W. SERPINB3 and B4: From biochemistry to biology. *Semin*

1149 *Cell Dev Biol.* **2017**, *Feb*, 170–177, doi:10.1016/j.semcdb.2016.09.005.
1150 35. Zhang Y, Wang L, Sun X, L.F. SERPINB4 Promotes Keratinocyte Inflammation via
1151 p38MAPK Signaling Pathway. *J Immunol Res.* **2023**, *Mar 21*,
1152 doi:10.1155/2023/3397940.
1153 36. Rigiracciolo DC, Nohata N, Lappano R, Cirillo F, Talia M, Adame-Garcia SR, Arang
1154 N, Lubrano S, De Francesco EM, Belfiore A, Gutkind JS, M.M. Focal Adhesion
1155 Kinase (FAK)-Hippo/YAP transduction signaling mediates the stimulatory effects
1156 exerted by S100A8/A9-RAGE system in triple-negative breast cancer (TNBC). *J Exp*
1157 *Clin Cancer Res.* **2022**, *Jun 3;41(1*, doi:10.1186/s13046-022-02396-0.
1158 37. Jumper J, Evans R, Pritzel A, Green T, Figurnov M, Ronneberger O, Tunyasuvunakool
1159 K, Bates R, Žídek A, Potapenko A, Bridgland A, Meyer C, Kohl SAA, Ballard AJ,
1160 Cowie A, Romera-Paredes B, Nikolov S, Jain R, Adler J, Back T, Petersen S, Reiman
1161 D, Clancy E, H.D. Highly accurate protein structure prediction with AlphaFold. *Nature*
1162 **2021**, *Aug;596*, 583–589, doi:10.1038/s41586-021-03819-2.
1163 38. Robert X, G.P. Deciphering key features in protein structures with the new ENDscript
1164 server. *Nucleic Acids Res.* **2014**, *Jul;42*, doi:10.1093/nar/gku316.
1165 39. Morsut, L.; Dupont, S.; Morsut, L.; Aragona, M.; Enzo, E.; Giulitti, S.; Cordenonsi, M.
1166 Role of YAP/TAZ in mechanotransduction. *Nature* **2011**, *474*, 179–183,
1167 doi:10.1038/nature10137.
1168 40. Kumar, M.; Gouw, M.; Michael, S.; Sámano-Sánchez, H.; Pancsa, R.; Glavina, J.;
1169 Diakogianni, A.; Valverde, J.A.; Bukirova, D.; Čalyševa, J.; et al. ELM—the
1170 eukaryotic linear motif resource in 2020. *Nucleic Acids Res.* **2019**,
1171 doi:10.1093/nar/gkz1030.
1172 41. Mészáros, B.; Erdős, G.; Dosztányi, Z. IUPred2A: context-dependent prediction of
1173 protein disorder as a function of redox state and protein binding. *Nucleic Acids Res.*
1174 **2018**, *46*, W329–W337, doi:10.1093/nar/gky384.
1175 42. De Munter, S.; Görnemann, J.; Derua, R.; Lesage, B.; Qian, J.; Heroes, E.; Waelkens,
1176 E.; Van Eynde, A.; Beullens, M.; Bollen, M. Split-BioID: a proximity biotinylation
1177 assay for dimerization-dependent protein interactions. *FEBS Lett.* 2017, *591*, 415–424.
1178 43. Schopp IM, Amaya Ramirez CC, Debeljak J, Kreibich E, Skribbe M, Wild K, B.J.
1179 Split-BioID a conditional proteomics approach to monitor the composition of
1180 spatiotemporally defined protein complexes. *Nat Commun.* **2017**, *Jun 6;8*,
1181 doi:10.1038/ncomms15690.
1182 44. Rakotoarison LM, Tebo AG, Böken D, Board S, El Hajji L, G.A. Improving Split

1183 Reporters of Protein-Protein Interactions through Orthology-Based Protein
1184 Engineering. *ACS Chem Biol.* **2024**, *Feb 16*, 428–441,
1185 doi:10.1021/acschembio.3c00631.
1186 45. Jia Y, Reboulet J, Gillet B, Hughes S, Forcet C, Tribollet V, Hajj Sleiman N, Kundlacz
1187 C, Vanacker JM, Bleicher F, M.S. A Live Cell Protein Complementation Assay for
1188 ORFeome-Wide Probing of Human HOX Interactomes. *Cells* **2023**, *12*, 200,
1189 doi:10.3390/cells12010200.
1190 46. Cox J, Neuhauser N, Michalski A, Scheltema RA, Olsen JV, M.M. Andromeda: a
1191 peptide search engine integrated into the MaxQuant environment. *J Proteome Res.*
1192 **2011**, *Apr 1;10*, 1794–805, doi:10.1021/pr101065j.
1193 47. Tyanova S, Temu T, C.J. The MaxQuant computational platform for mass
1194 spectrometry-based shotgun proteomics. *Nat Protoc.* **2016**, *Dec;11*, 2301–2319,
1195 doi:10.1038/nprot.2016.136.
1196 48. Szklarczyk D, Gable AL, Nastou KC, Lyon D, Kirsch R, Pyysalo S, Doncheva NT,
1197 Legeay M, Fang T, Bork P, Jensen LJ, von M.C. The STRING database in 2021:
1198 customizable protein-protein networks, and functional characterization of user-
1199 uploaded gene/measurement sets. *Nucleic Acids Res.* **2021**, *Jan 8;49*, D605–D612,
1200 doi:10.1093/nar/gkaa1074.
1201 49. Shannon, P., Markiel, A., Ozier, O., Baliga, N.S., Wang, J.T., Ramage, D., Amin, N.,
1202 Schwikowski, B., and Ideker, T. Shannon, P., Markiel, A., Ozier, O., Baliga, N.S.,
1203 Wang, J.T., Ramage, D., Amin, N., Schwikowski, B., and Ideker, T. Cytoscape: a
1204 software environment for integrated models of biomolecular interaction networks.
1205 *Genome Res.* **2003**, *13*, 2498–2504.
1206 50. Thomas PD, Ebert D, Muruganujan A, Mushayahama T, Albou LP, M.H. PANTHER:
1207 Making genome-scale phylogenetics accessible to all. *Protein Sci.* **2022**, *Jan;31*, 8–22,
1208 doi:10.1002/pro.4218.
1209 51. Smith T, Heger A, S.I. UMI-tools: modeling sequencing errors in Unique Molecular
1210 Identifiers to improve quantification accuracy. *Genome Res.* **2017**, *Mar;27*, 491–499,
1211 doi:10.1101/gr.209601.116.
1212 52. Kechin A, Boyarskikh U, Kel A, F.M. cutPrimers: A New Tool for Accurate Cutting
1213 of Primers from Reads of Targeted Next Generation Sequencing. *J Comput Biol.* **2017**,
1214 *Nov;24*, 1138–1143, doi:10.1089/cmb.2017.0096.
1215 53. Dobin A, Davis CA, Schlesinger F, Drenkow J, Zaleski C, Jha S, Batut P, Chaisson M,
1216 G.T. STAR: ultrafast universal RNA-seq aligner. *Bioinformatics.* **2013**, *Jan 1;29*, 15–

21, doi:10.1093/bioinformatics/bts635.

54. Anders S, Pyl PT, H.W. HTSeq--a Python framework to work with high-throughput sequencing data. *Bioinformatics.* **2015**, *Jan 15;31*, 166–9, doi:10.1093/bioinformatics/btu638.

55. Love MI, Huber W, A.S. Moderated estimation of fold change and dispersion for RNA-seq data with DESeq2. *Genome Biol.* **2014**, *15(12)*, doi:10.1186/s13059-014-0550-8.

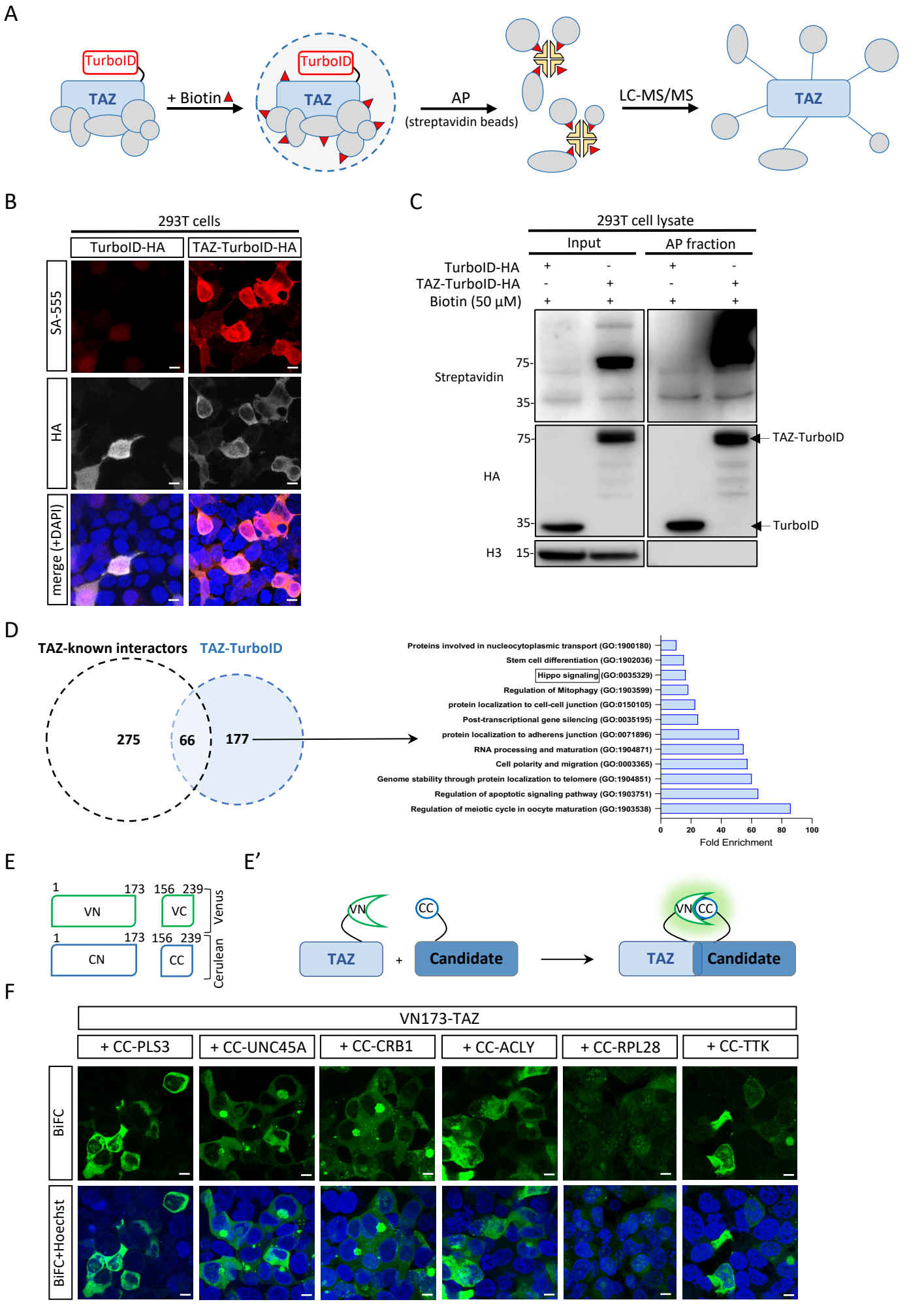
A
TurboID
TAZ
+ Biotin
TurboID
TAZ
AP
(streptavidin beads)
LC-MS/MS
TAZ
B
293T cells
TurboID-HA
TAZ-TurboID-HA
SA-555
HA
merge (+DAPI)
C
293T cell lysate
Input
AP fraction
TurboID-HA
TAZ-TurboID-HA
Biotin (50 µM)
Streptavidin
75-
35-
HA
75-
35-
TAZ-TurboID
TurboID
H3
15-
D
TAZ-known interactors
TAZ-TurboID
275
66
177
Proteins involved in nucleocytoplasmic transport (GO:1900180)
Stem cell differentiation (GO:1902036)
Hippo signaling (GO:0035329)
Regulation of Mitophagy (GO:1903599)
protein localization to cell-cell junction (GO:0150105)
Post-transcriptional gene silencing (GO:0035195)
protein localization to adherens junction (GO:0071896)
RNA processing and maturation (GO:1904871)
Cell polarity and migration (GO:0003365)
Genome stability through protein localization to telomere (GO:1904851)
Regulation of apoptotic signaling pathway (GO:1903751)
Regulation of meiotic cycle in oocyte maturation (GO:1903538)
0
20
40
60
80
100
Fold Enrichment
E
1
173
156
239
VN
VC
Venus
1
173
156
239
CN
CC
Cerulean
E'
VN
CC
TAZ
+
Candidate
VN
CC
TAZ
Candidate
F
VN173-TAZ
+ CC-PLS3
+ CC-UNC45A
+ CC-CRB1
+ CC-ACLY
+ CC-RPL28
+ CC-TTK
BiFC
BiFC+Hoechst

Figure 1

A

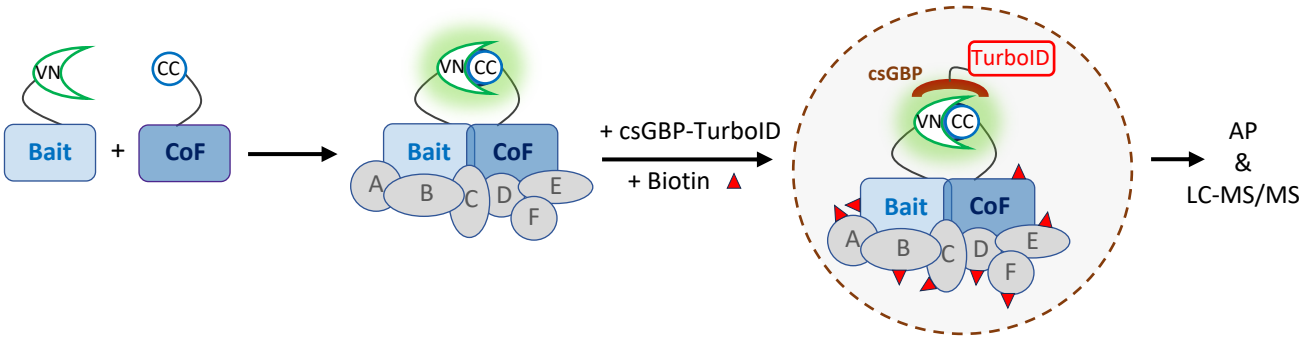

B

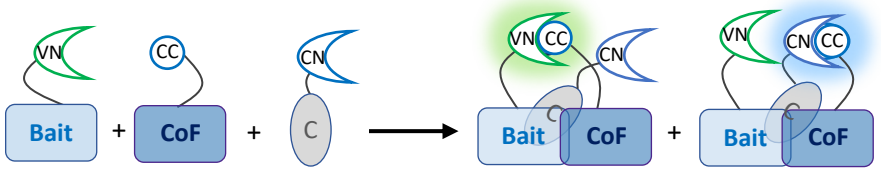

C

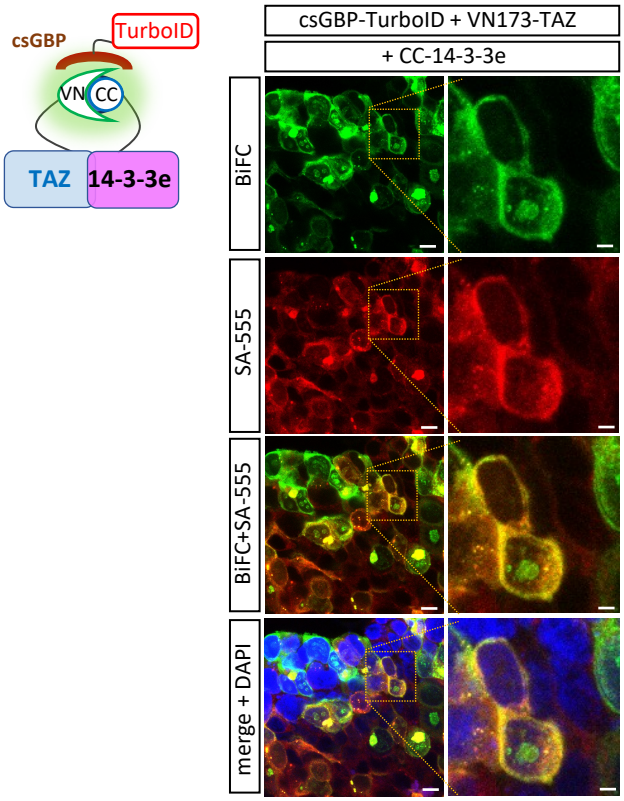

D

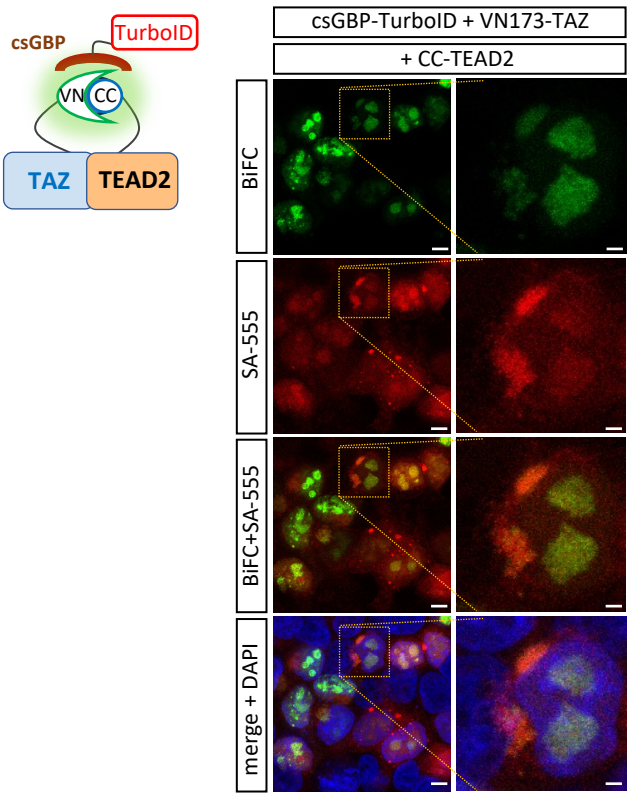

E

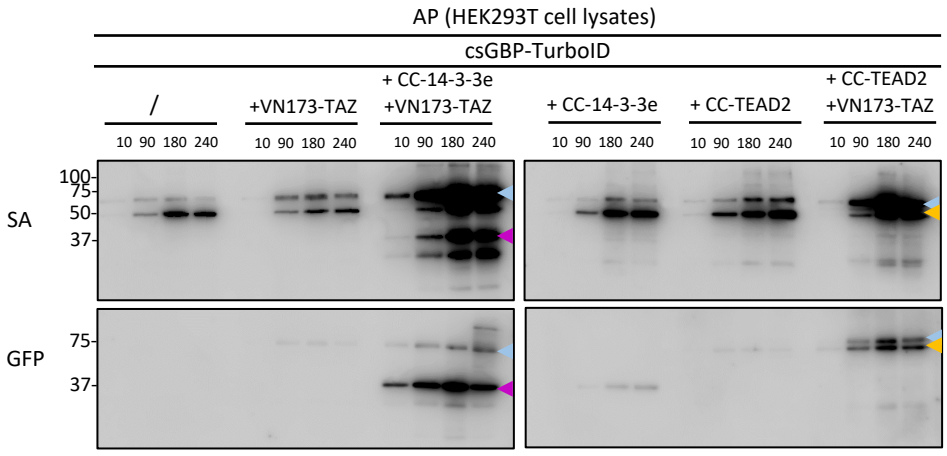

E'

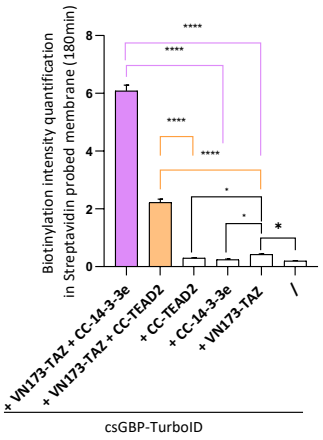

Figure 2

A

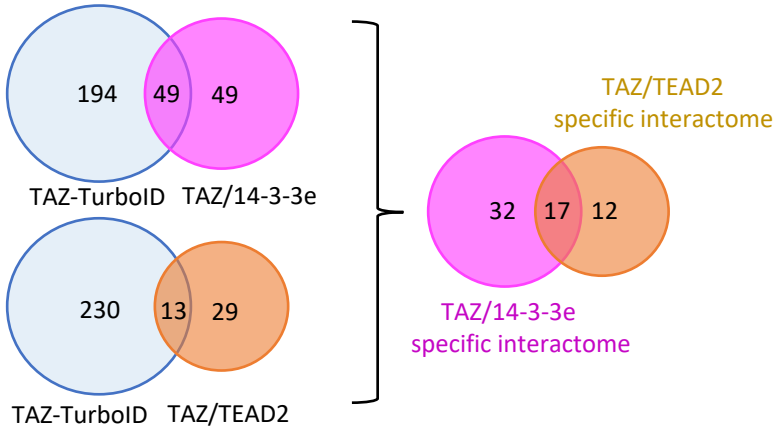

B

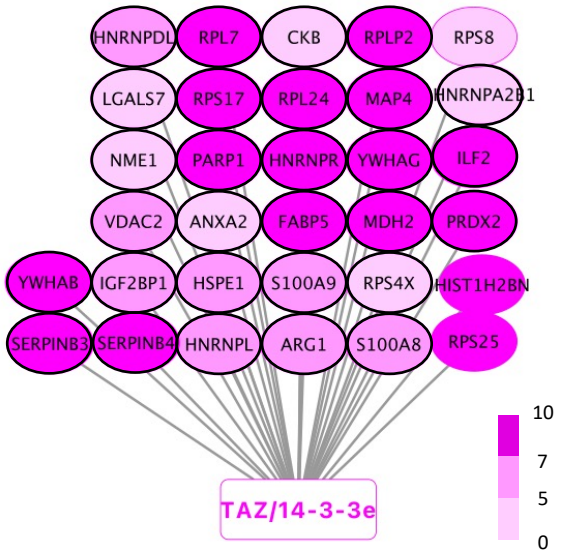

B'

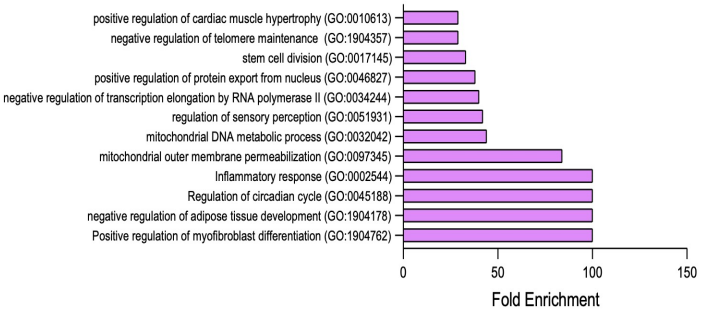

C

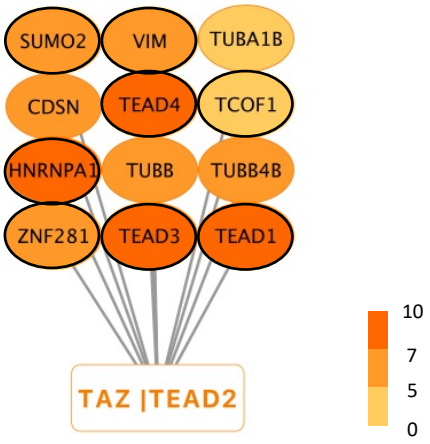

C'

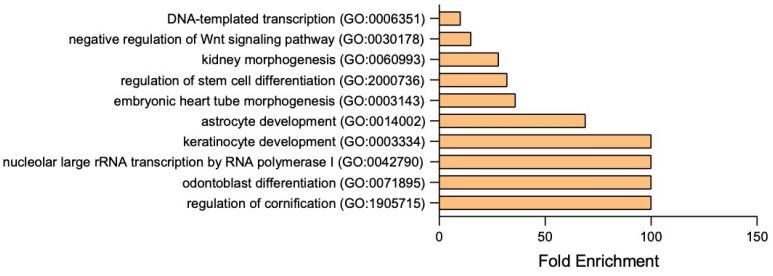

Figure 3

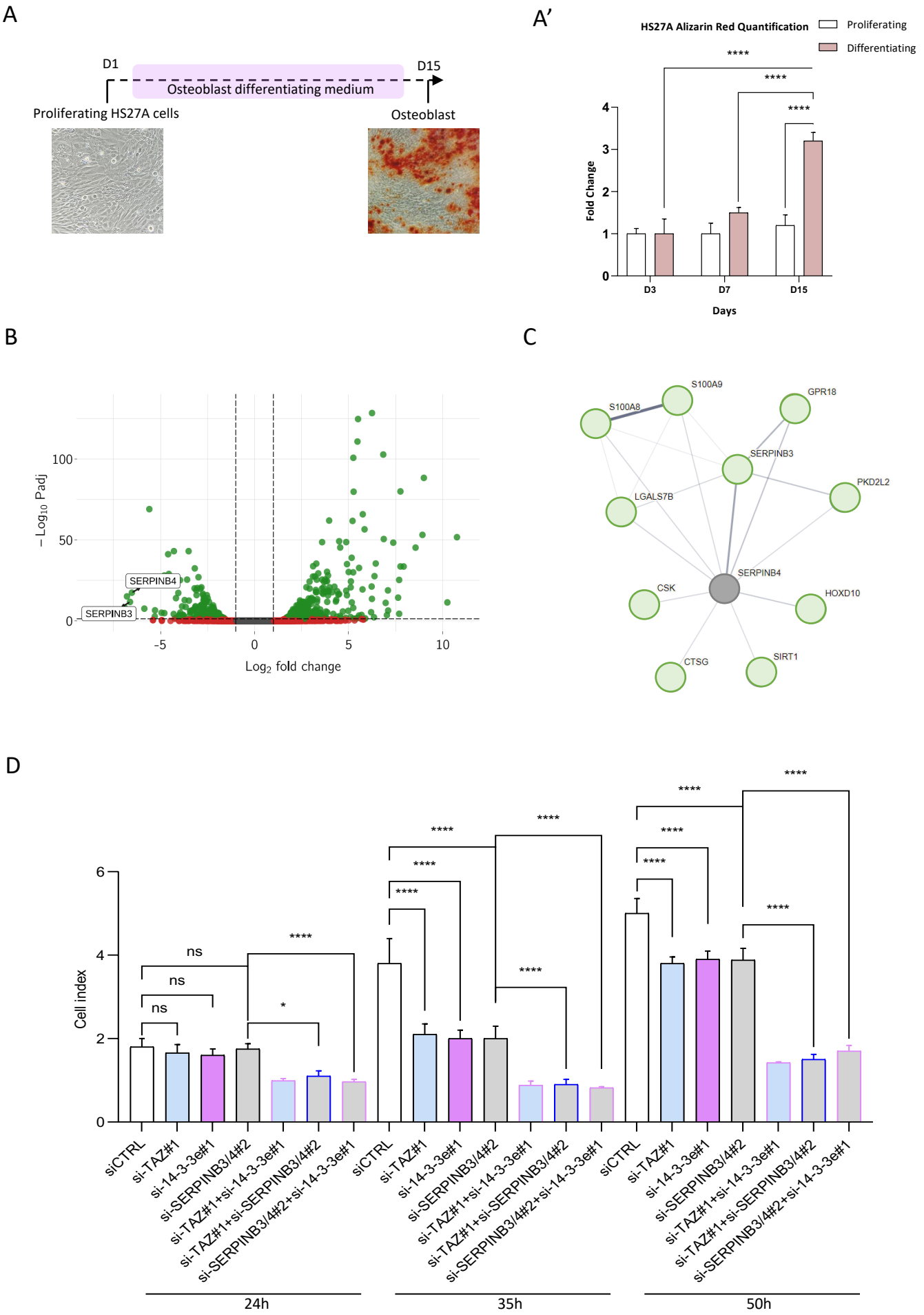
A
D1
D15
Osteoblast differentiating medium
Proliferating HS27A cells
Osteoblast
A'
HS27A Alizarin Red Quantification
Proliferating
Differentiating
Fold Change
Days
D3
D7
D15
B
SERPINB4
SERPINB3
Log2 fold change
C
S100A9
S100A8
GPR18
SERPINB3
PKD2L2
LGALS7B
SERPINB4
CSK
HOXD10
CTSG
SIRT1
D
Cell index
siCTRL
si-TAZ#1
si-14-3-3e#1
si-SERPINB3/4#2
si-TAZ#1+si-14-3-3e#1
si-TAZ#1+si-SERPINB3/4#2
si-SERPINB3/4#2+si-14-3-3e#1
24h
35h
50h

Figure 4

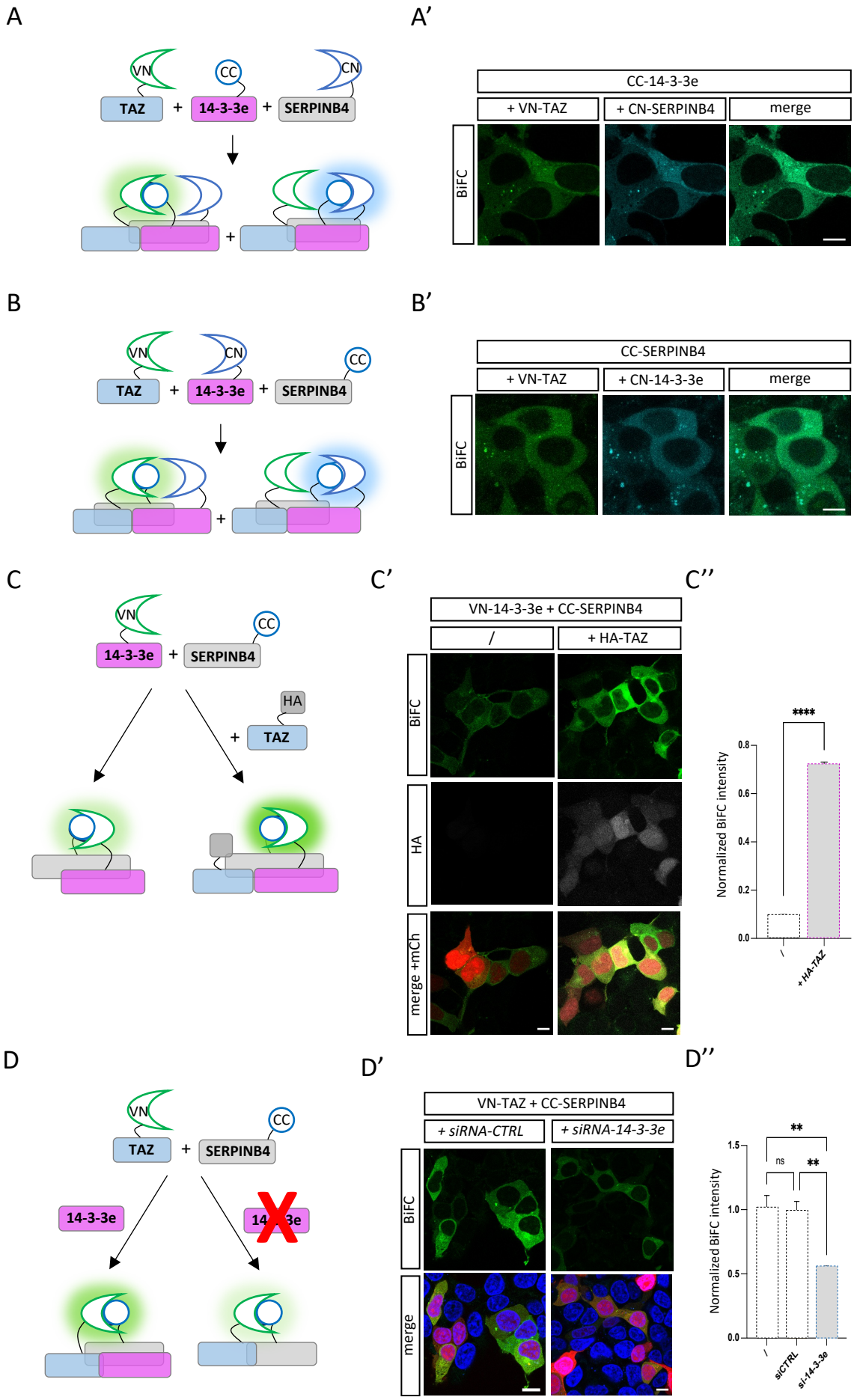
A
VN
CC
CN
TAZ
14-3-3e
SERPINB4
A'
CC-14-3-3e
+ VN-TAZ
+ CN-SERPINB4
merge
BiFC
B
VN
CN
CC
TAZ
14-3-3e
SERPINB4
B'
CC-SERPINB4
+ VN-TAZ
+ CN-14-3-3e
merge
BiFC
C
VN
CC
14-3-3e
SERPINB4
HA
TAZ
C'
VN-14-3-3e + CC-SERPINB4
/
+ HA-TAZ
BiFC
HA
merge +mCh
C''
****
Normalized BiFC intensity
0.8
0.6
0.4
0.2
0.0
/
+ HA-TAZ
D
VN
CC
TAZ
SERPINB4
14-3-3e
D'
VN-TAZ + CC-SERPINB4
+ siRNA-CTRL
+ siRNA-14-3-3e
BiFC
merge
D''
**
ns
**
Normalized BiFC intensity
1.5
1.0
0.5
0.0
/
siCTRL
si-14-3-3e

Figure 5

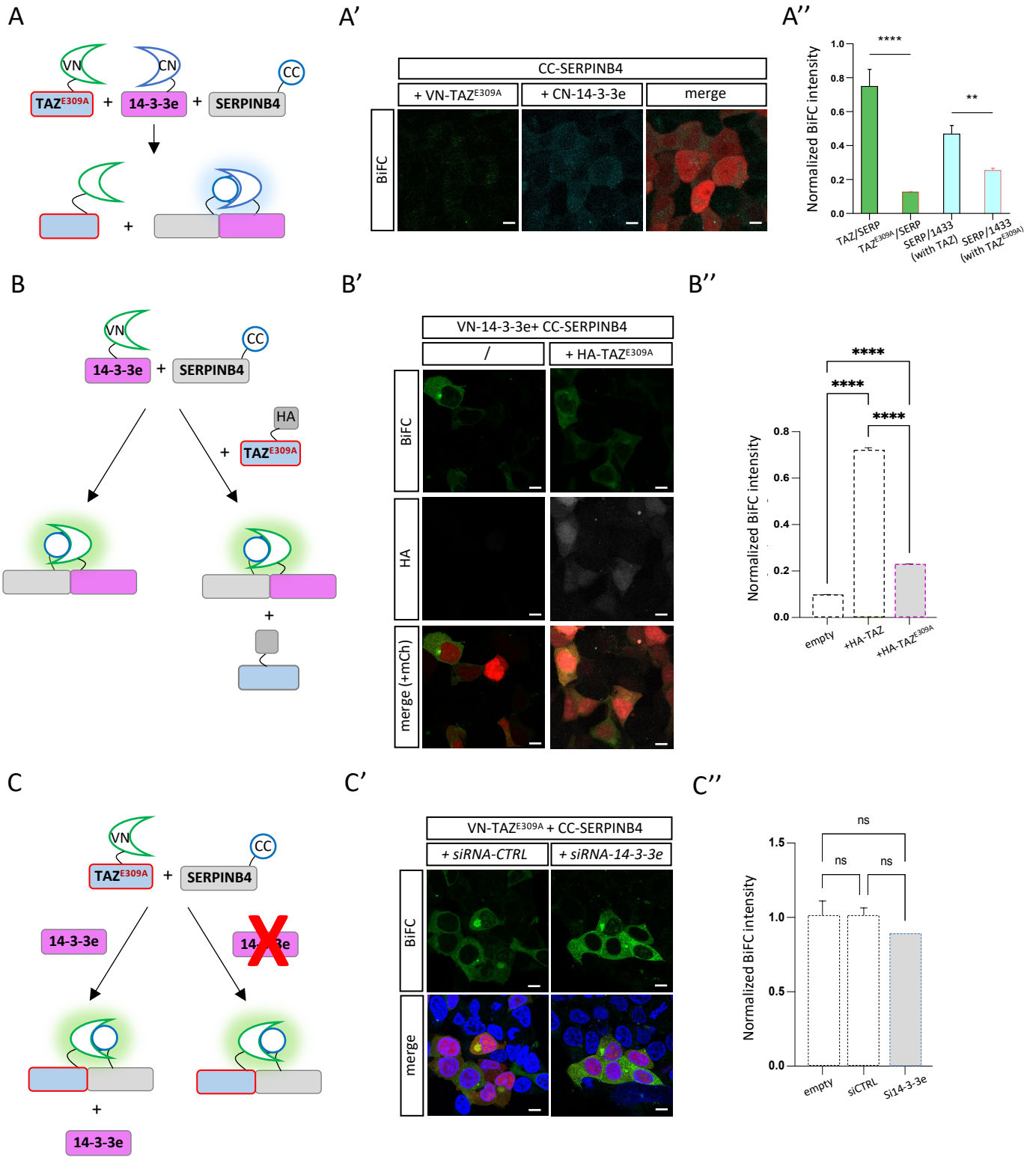
A
VN
CN
CC
TAZE309A
+
14-3-3e
+
SERPINB4
A'
CC-SERPINB4
+ VN-TAZE309A
+ CN-14-3-3e
merge
BiFC
A''
Normalized BiFC intensity
****
**
TAZ/SERP
TAZE309A/SERP
SERP/1433 (with TAZ)
SERP/1433 (with TAZE309A)
B
VN
CC
14-3-3e
+
SERPINB4
HA
+
TAZE309A
B'
VN-14-3-3e+ CC-SERPINB4
/
+ HA-TAZE309A
BiFC
HA
merge (+mCh)
B''
Normalized BiFC intensity
****
****
****
empty
+HA-TAZ
+HA-TAZE309A
C
VN
CC
TAZE309A
+
SERPINB4
14-3-3e
14-3-3e
+
14-3-3e
C'
VN-TAZE309A + CC-SERPINB4
+ siRNA-CTRL
+ siRNA-14-3-3e
BiFC
merge
C''
Normalized BiFC intensity
ns
ns
ns
empty
siCTRL
Si14-3-3e

Figure 6

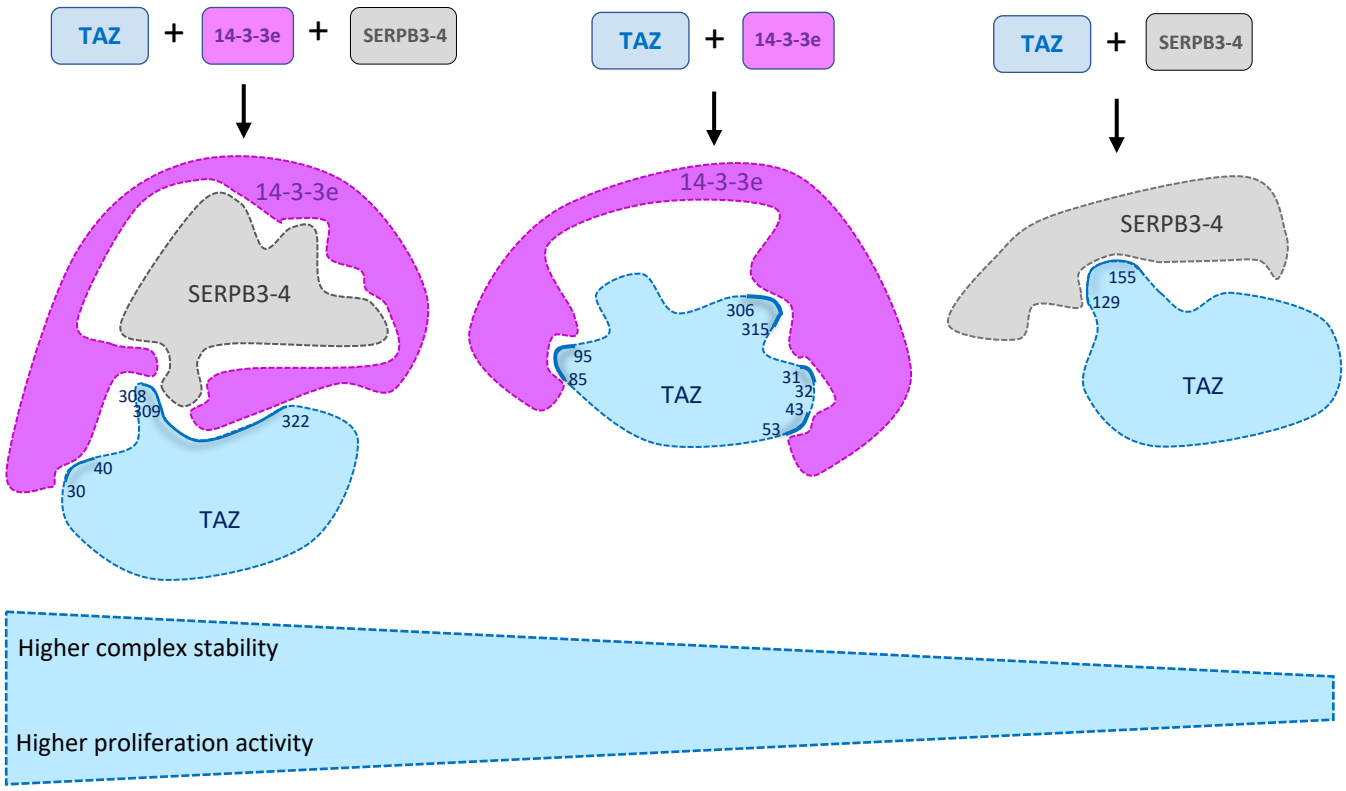
TAZ
+
14-3-3e
+
SERPB3-4
14-3-3e
SERPB3-4
308
309
322
40
30
TAZ
TAZ
+
14-3-3e
14-3-3e
306
315
95
85
TAZ
31
32
43
53
TAZ
+
SERPB3-4
SERPB3-4
155
129
TAZ
Higher complex stability
Higher proliferation activity

Figure 7

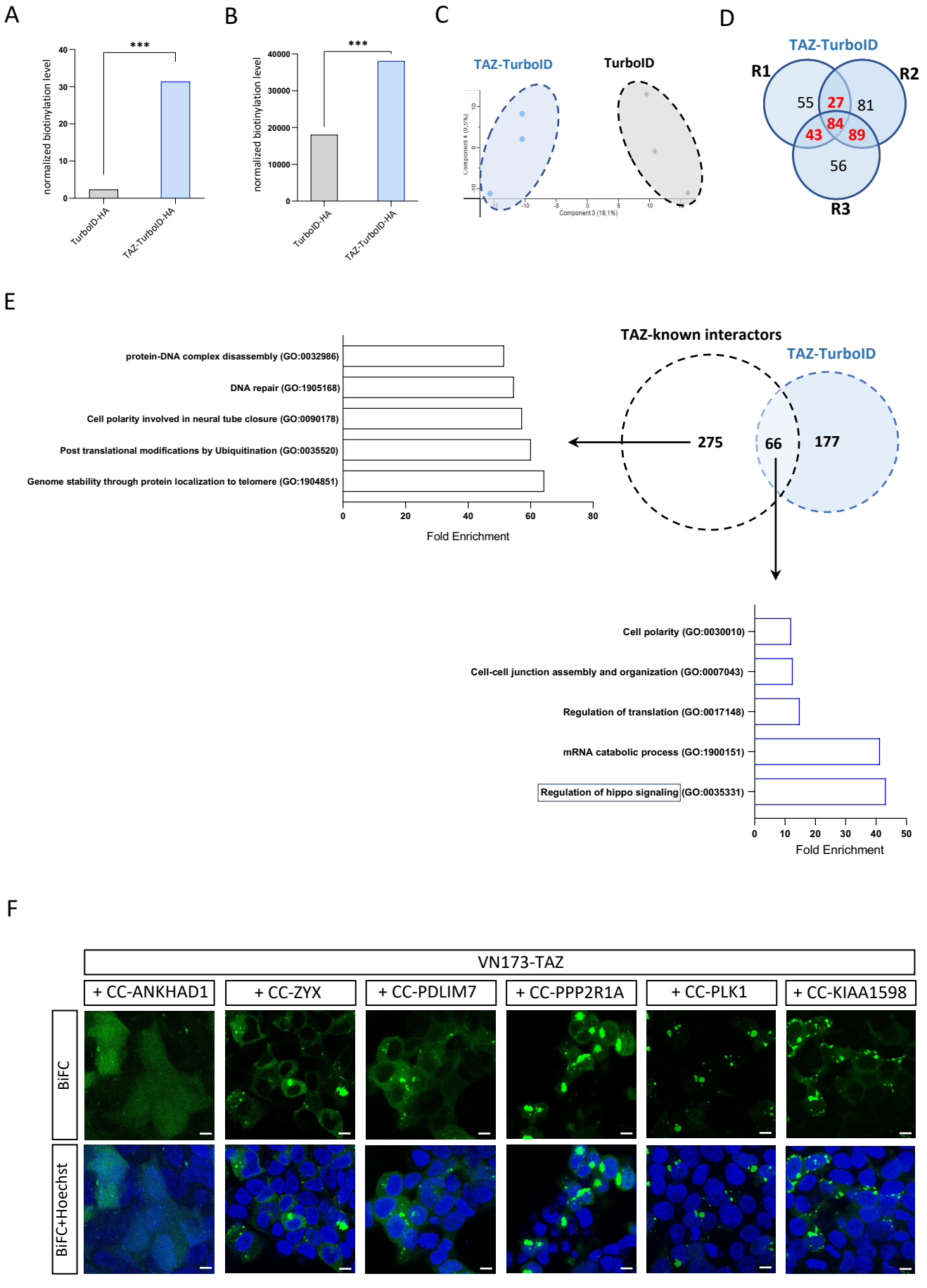

Supplementary Figure 1

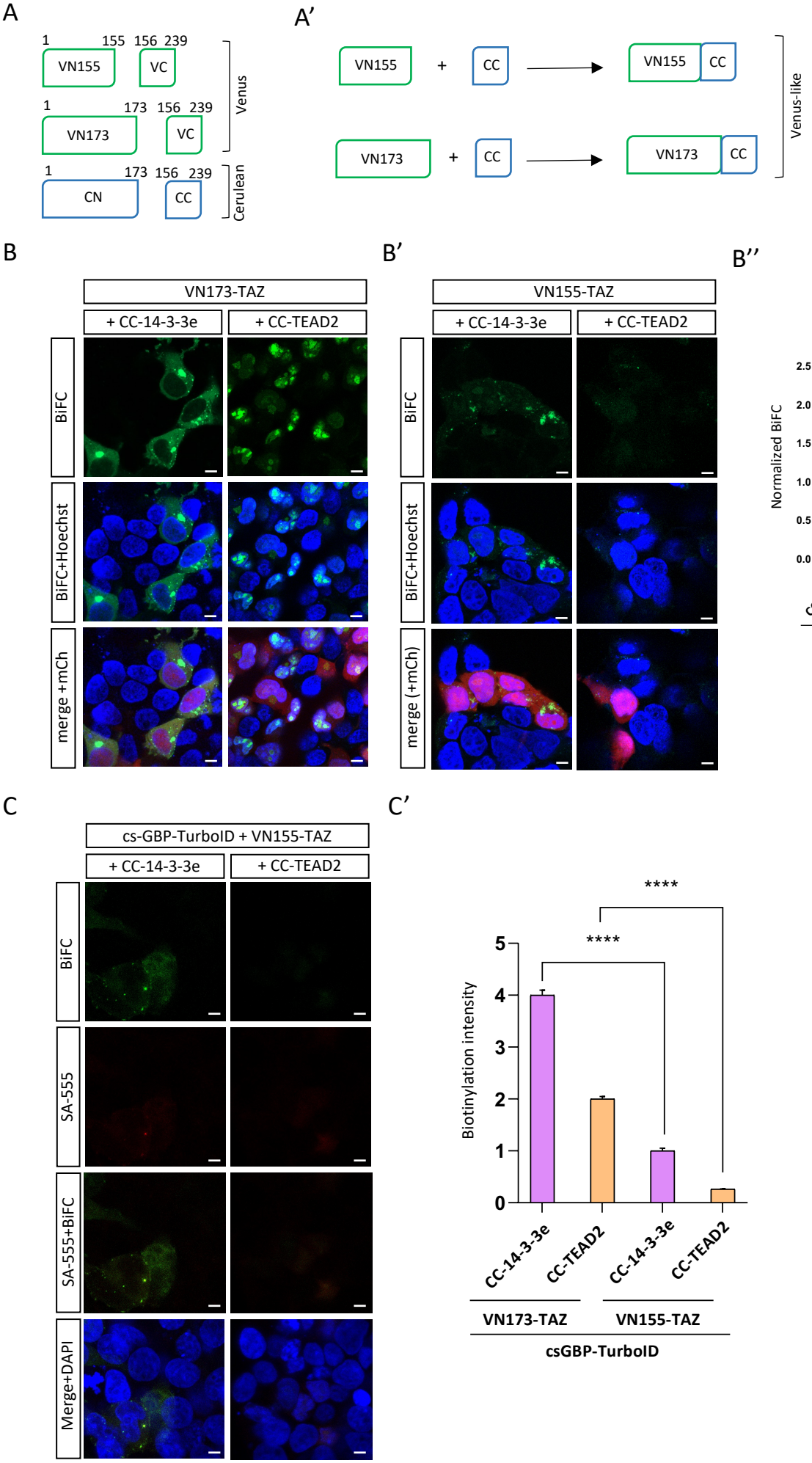

Supplementary Figure 2

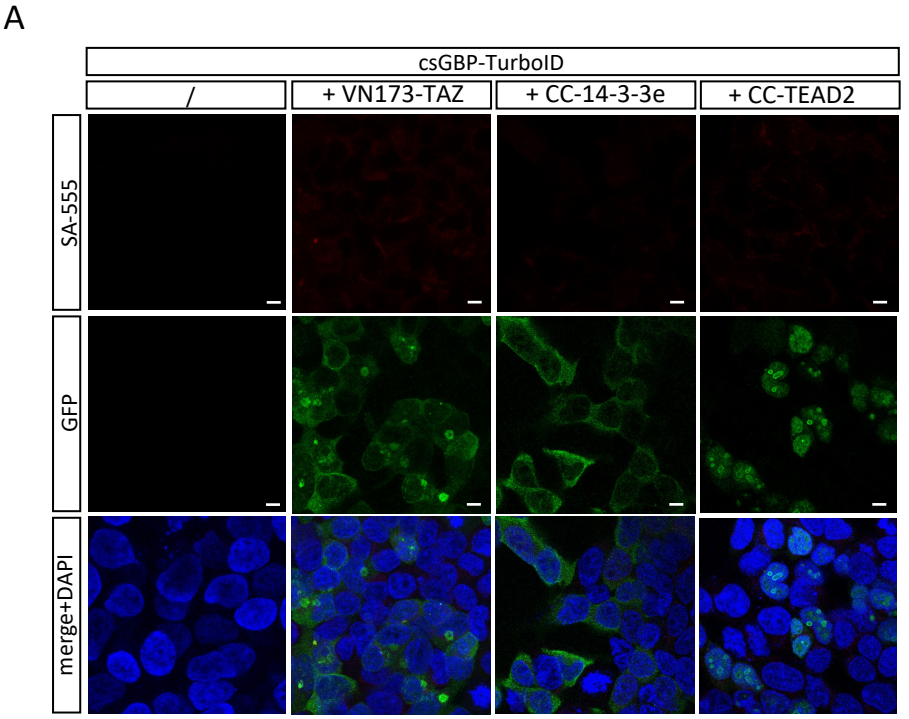

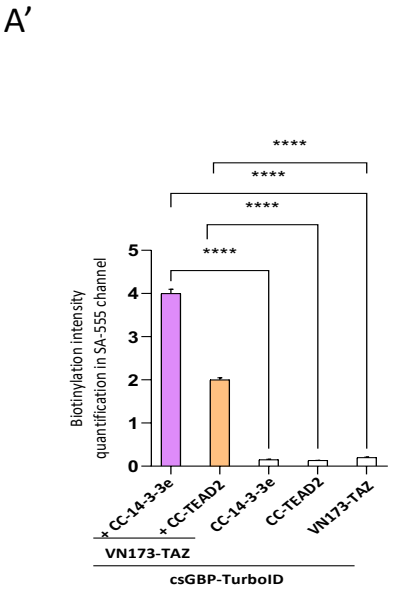

Supplementary Figure 3

A

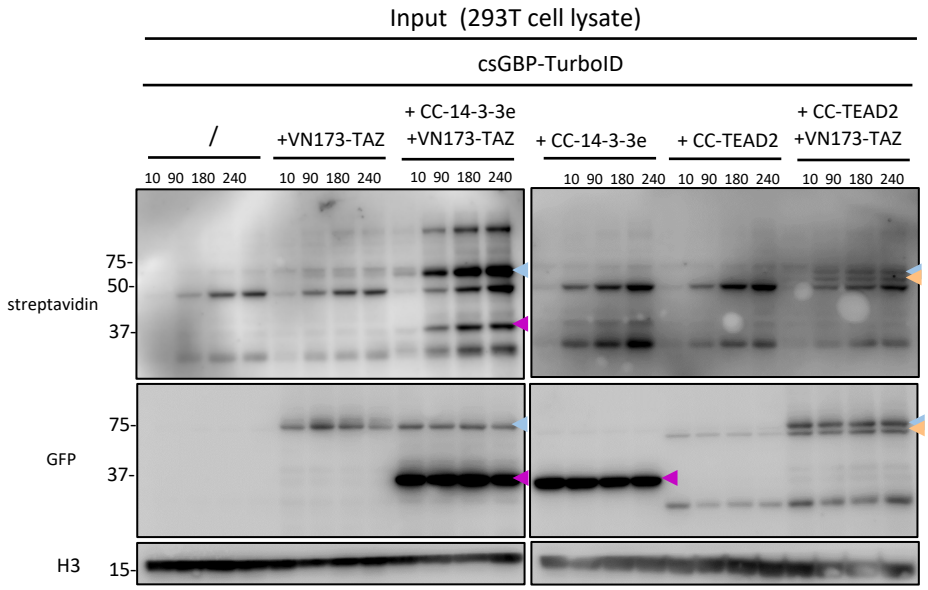

A'

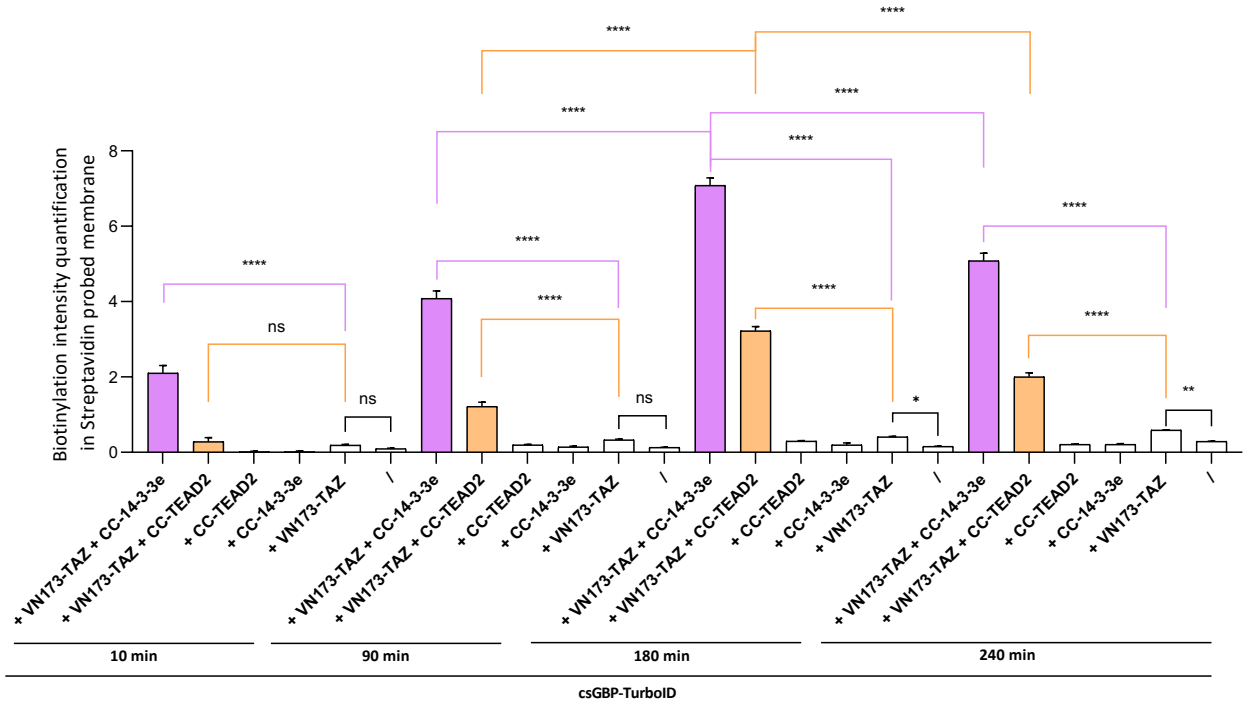

Supplementary Figure 4

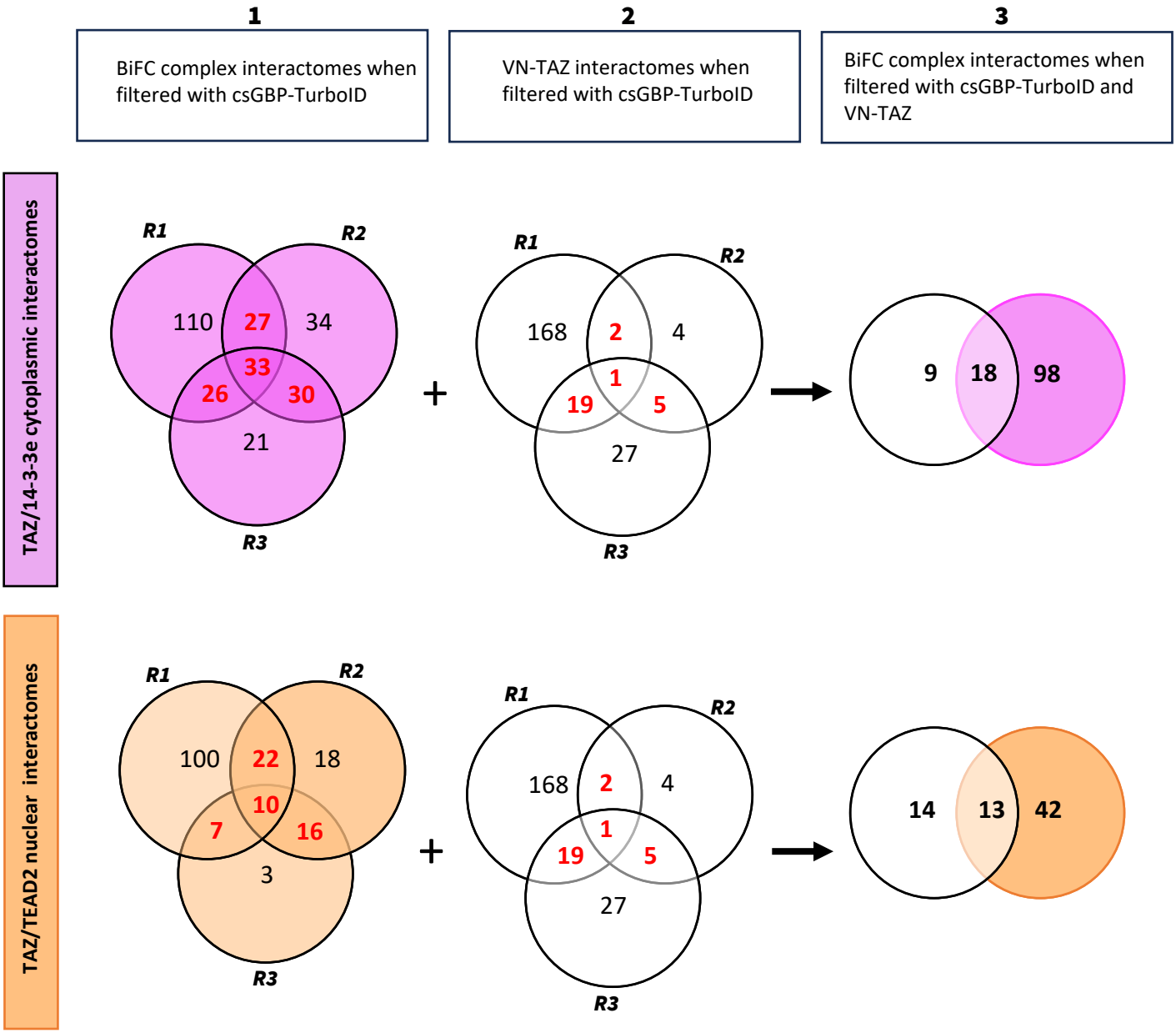

Supplementary Figure 5

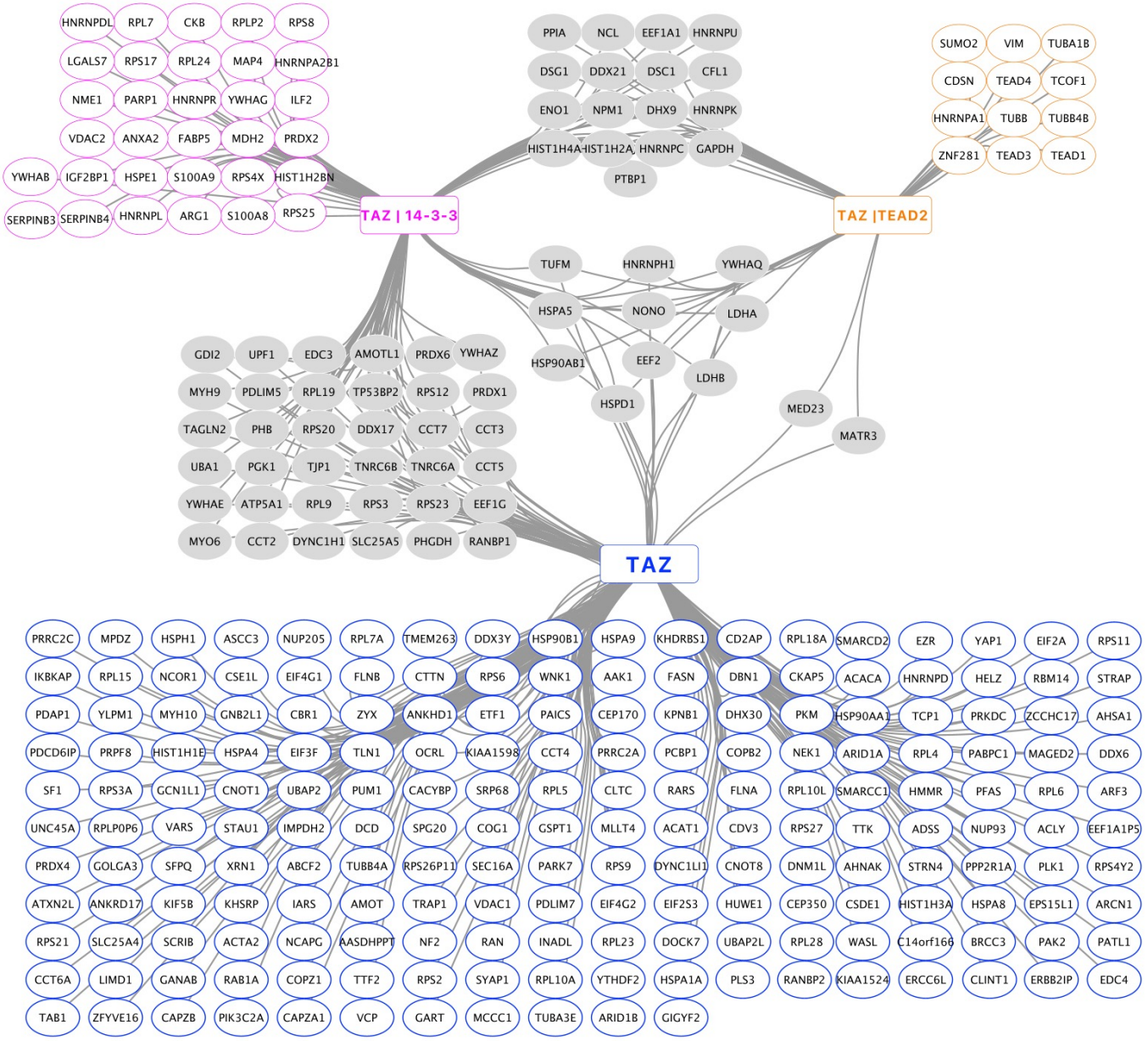

Supplementary Figure 6

Supplementary Figure 7

```
                    10        20        30        40        50        60
                     |         |         |         |         |         |
SERPINB3     MNSLSEANTKFMFDLFQQFRKSKENNIFYSPISITSALGMVLLGAKDNTAQQIKKVLHFD
SERPINB4     MNSLSEANTKFMFDLFQQFRKSKENNIFYSPISITSALGMVLLGAKDNTAQQISKVLHFD
             ***************************************************.******
Prim.cons.   MNSLSEANTKFMFDLFQQFRKSKENNIFYSPISITSALGMVLLGAKDNTAQQI2KVLHFD

                    70        80        90       100       110       120
                     |         |         |         |         |         |
SERPINB3     QVTENTTGKAATYHVDRSGNVHHQFQKLLTEFNKSTDAYELKIANKLFGEKTYLFLQEYL
SERPINB4     QVTENTTEKAATYHVDRSGNVHHQFQKLLTEFNKSTDAYELKIANKLFGEKTYQFLQEYL
             ******* ********************************************* ******
Prim.cons.   QVTENTT2KAATYHVDRSGNVHHQFQKLLTEFNKSTDAYELKIANKLFGEKTY2FLQEYL

                   130       140       150       160       170       180
                     |         |         |         |         |         |
SERPINB3     DAIKKFYQTSVESVDFANAPEESRKKINSWVESQTNEKIKNLIPEGNIGSNTTLVLVNAI
SERPINB4     DAIKKFYQTSVESTDFANAPEESRKKINSWVESQTNEKIKNLFPDGTIGNDTTLVLVNAI
             *************.****************************:*:*.**.:*********
Prim.cons.   DAIKKFYQTSVES2DFANAPEESRKKINSWVESQTNEKIKNL2P2G2IG22TTLVLVNAI

                   190       200       210       220       230       240
                     |         |         |         |         |         |
SERPINB3     YFKGQWEKKFNKEDTKEEKFWPNKNTYKSIQMMRQYTSFHFASLEDVQAKVLEIPYKGKD
SERPINB4     YFKGQWENKFKKENTKEEKFWPNKNTYKSVQMMRQYNSFNFALLEDVQAKVLEIPYKGKD
             *******:**:**:***************:******.**:** *****************
Prim.cons.   YFKGQWE2KF2KE2TKEEKFWPNKNTYKS2QMMRQY2SF2FA2LEDVQAKVLEIPYKGKD

                   250       260       270       280       290       300
                     |         |         |         |         |         |
SERPINB3     LSMIVLLPNEIDGLQKLEEKLTAEKLMEWTSLQNMRETRVDLHLPRFKVEESYDLKDTLR
SERPINB4     LSMIVLLPNEIDGLQKLEEKLTAEKLMEWTSLQNMRETCVDLHLPRFKMEESYDLKDTLR
             ************************************** *********:***********
Prim.cons.   LSMIVLLPNEIDGLQKLEEKLTAEKLMEWTSLQNMRET2VDLHLPRFK2EESYDLKDTLR

                   310       320       330       340       350       360
                     |         |         |         |         |         |
SERPINB3     TMGMVDIFNGDADLSGMTGSRGLVLSGVLHKAFVEVTEEGAEAAAATAVVGFGSSPTSTN
SERPINB4     TMGMVNIFNGDADLSGMTWSHGLSVSKVLHKAFVEVTEEGVEAAAATAVVVVELSSPSTN
             *****:************ *:** :* *************.********* .  *..***
Prim.cons.   TMGMV2IFNGDADLSGMT2S2GL22S2VLHKAFVEVTEEG2EAAAATAVV2222S22STN

                   370       380       390
                     |         |         |
SERPINB3     EEFHCNHPFLFFIRQNKTNSILFYGRFSSP
SERPINB4     EEFCCNHPFLFFIRQNKTNSILFYGRFSSP
             *** **************************
Prim.cons.   EEF2CNHPFLFFIRQNKTNSILFYGRFSSP
```

Supplementary Figure 8

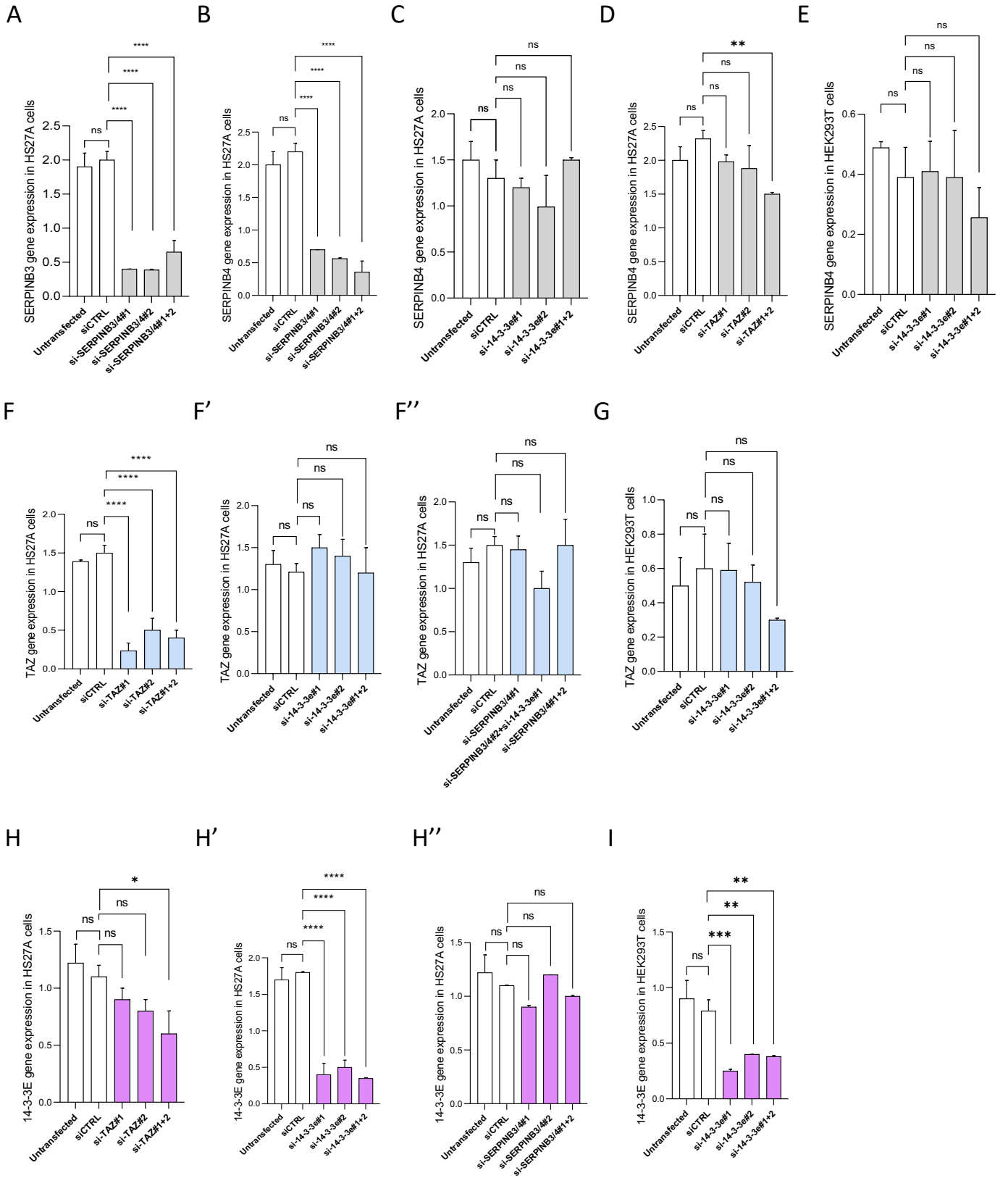

Supplementary Figure 9

A

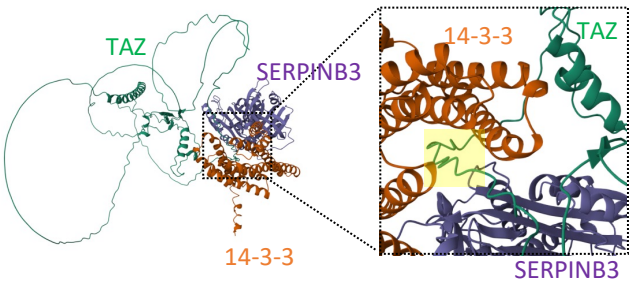

B

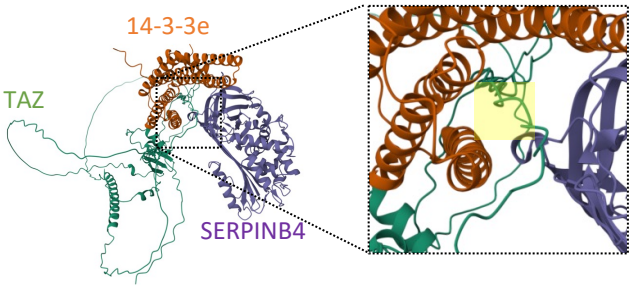

C

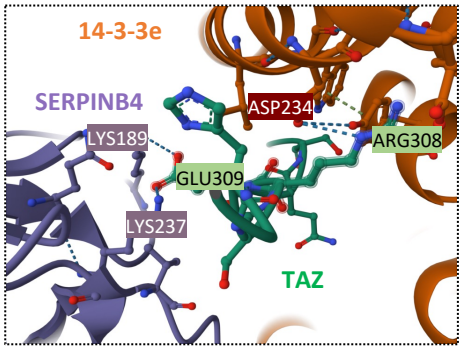

D

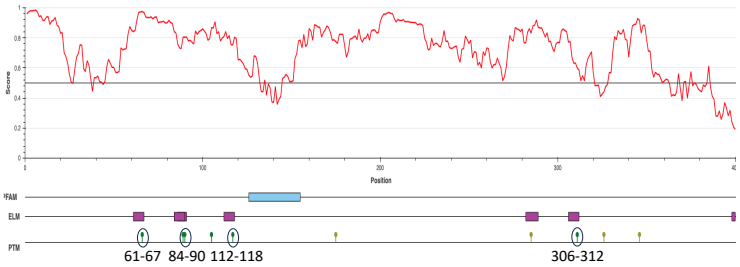

E

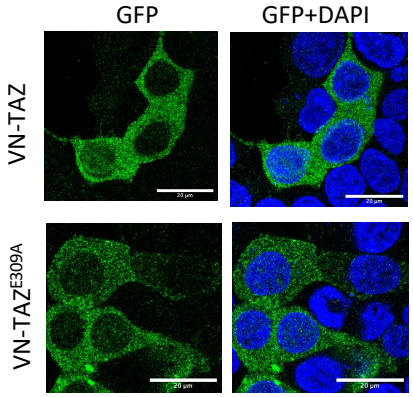

E'

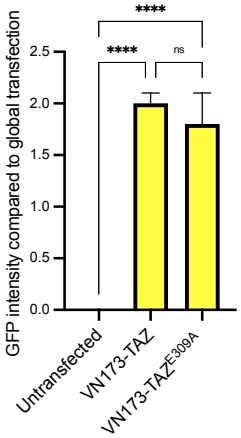

Supplementary Figure 10

A

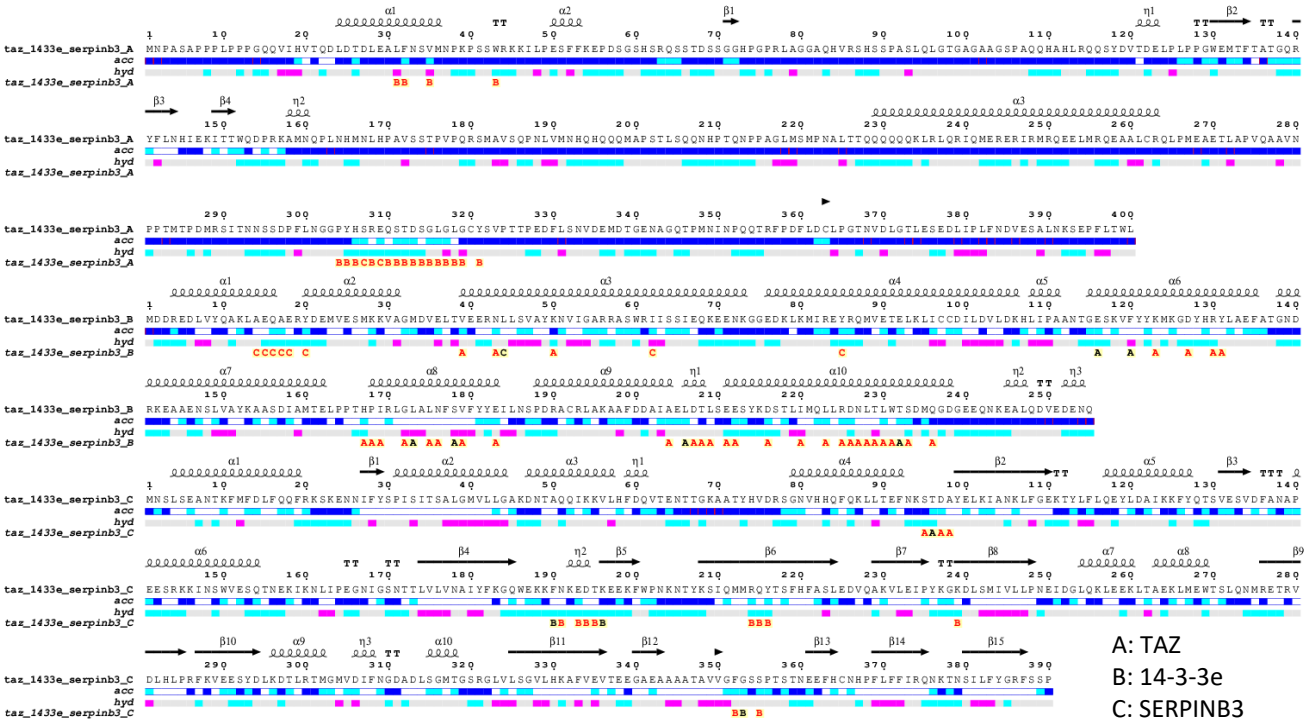

B

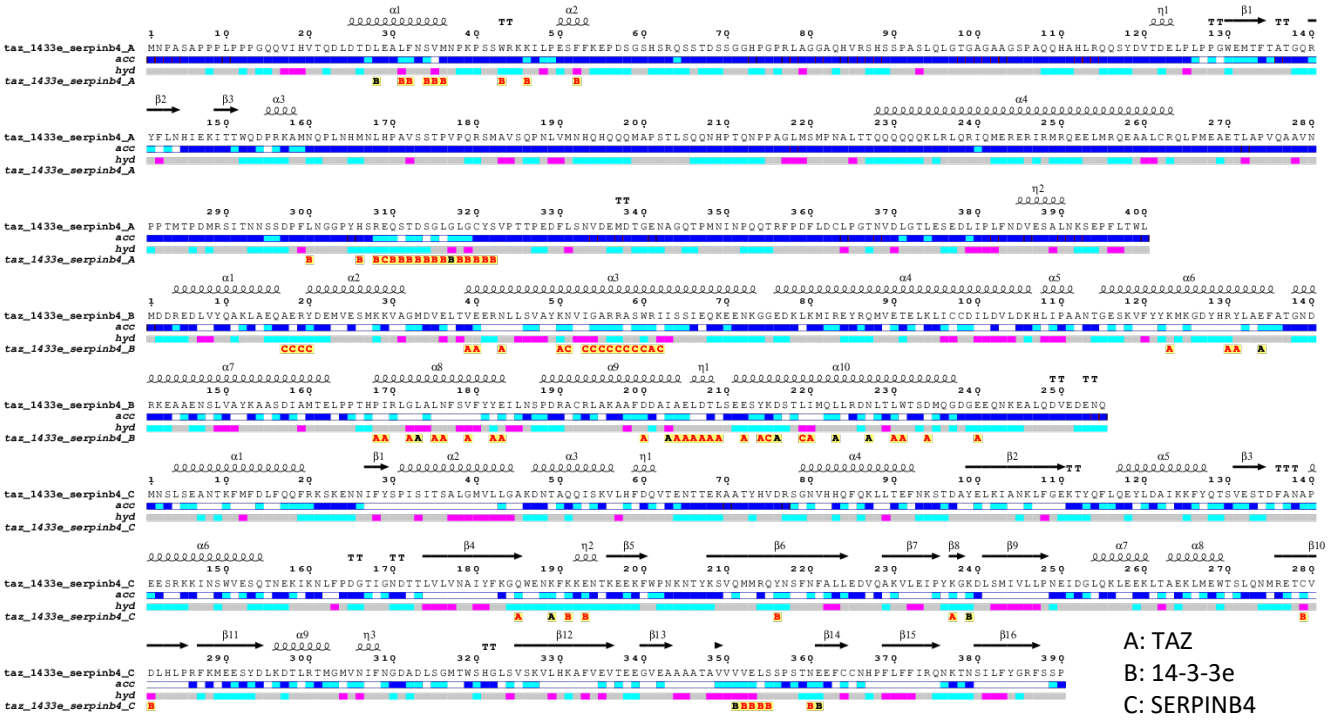

Supplementary Figure 11

A

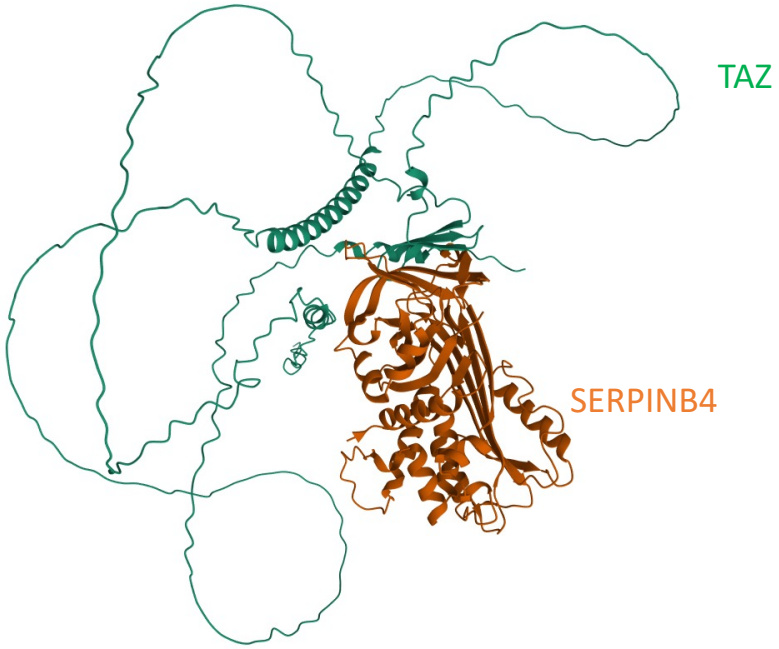

B

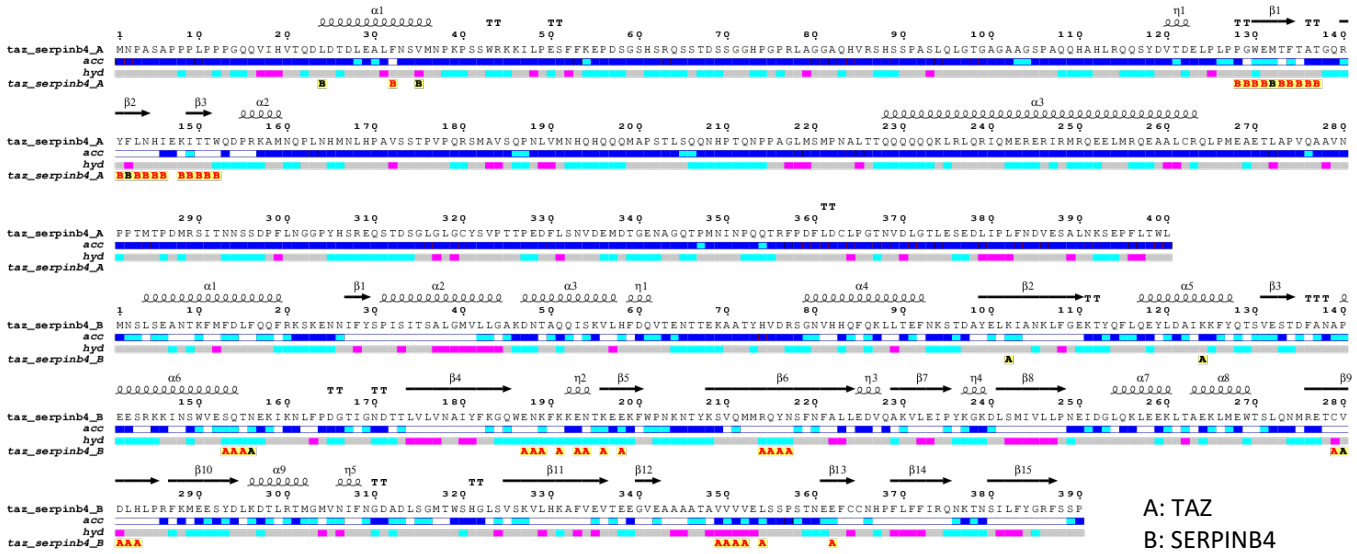

Supplementary Figure 12

A

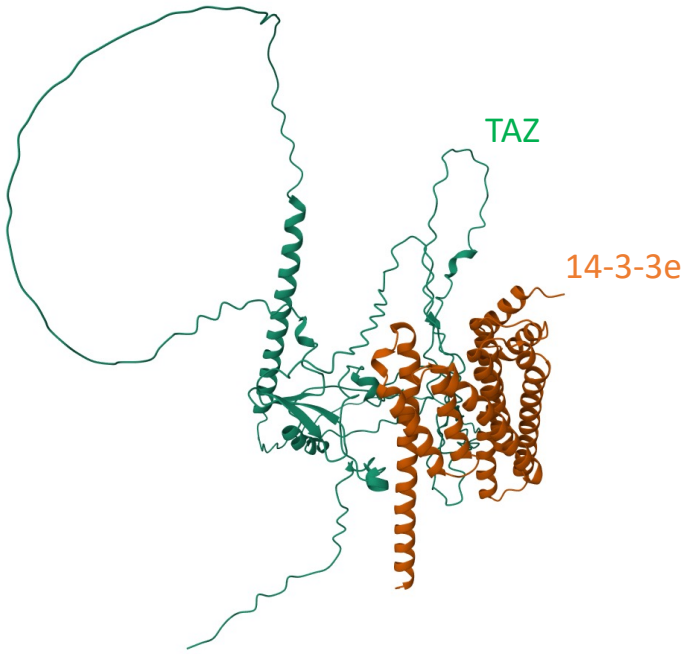

B

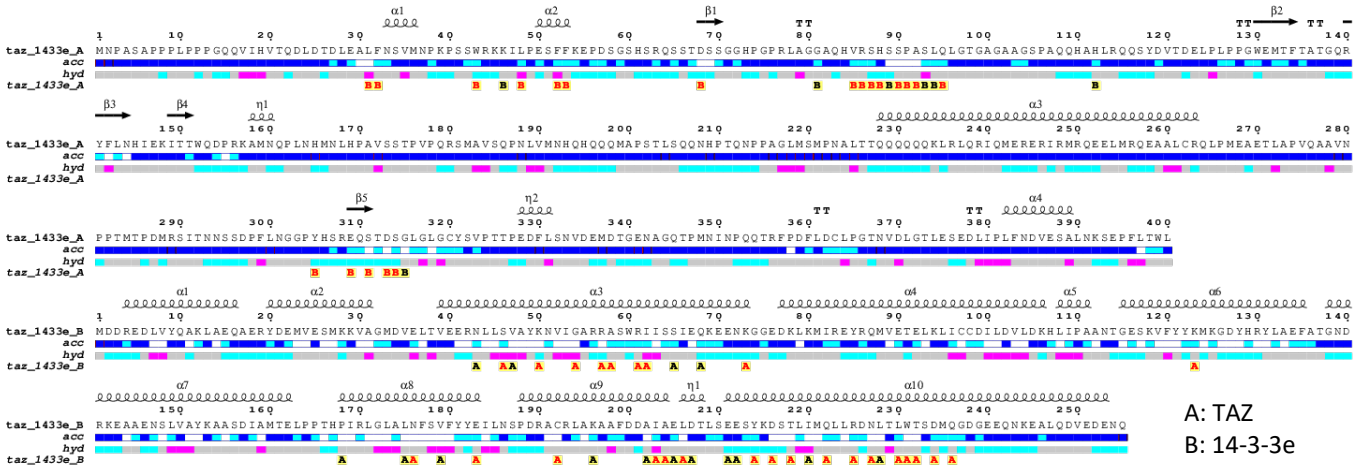

Supplementary Figure 13

A

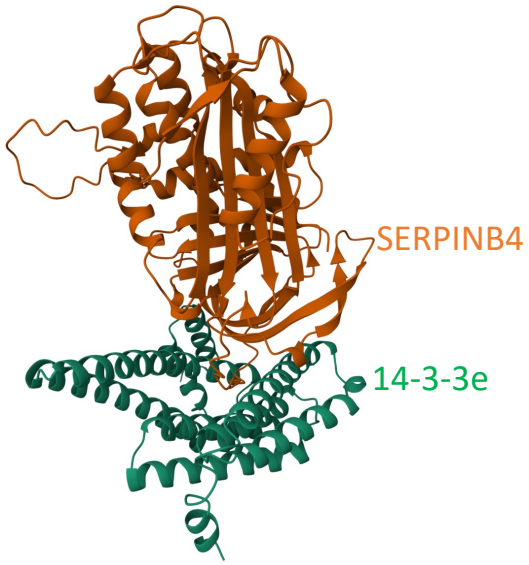

B

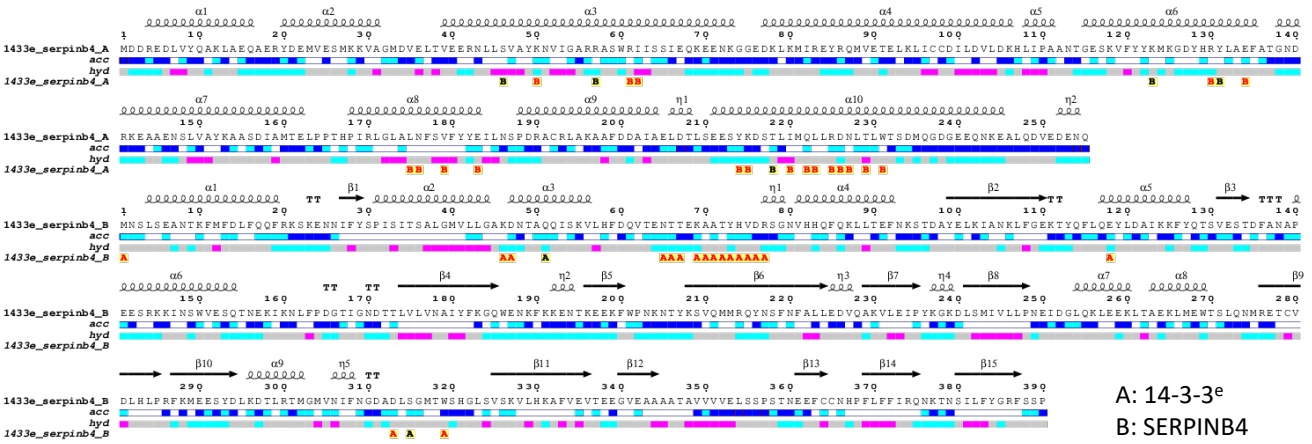

Supplementary Figure 14